

DESIGN OF A ROBOTIC CANNULA FOR ROBOTIC LUMBAR DISCECTOMY

A Dissertation

Submitted to the Faculty

of

Purdue University

by

Yang Ding

In Partial Fulfillment of the

Requirements for the Degree

of

Master of Science in Mechanical Engineering

August 2019

Purdue University

West Lafayette, Indiana

THE PURDUE UNIVERSITY GRADUATE SCHOOL
STATEMENT OF DISSERTATION APPROVAL

Dr. David J. Cappelleri, Chair

School of Mechanical Engineering

Dr. George T. C. Chiu

School of Mechanical Engineering

Dr. Raymond J. Cipra

School of Mechanical Engineering

Approved by:

Dr. Jay P. Gore

Head of the School Graduate Program

TABLE OF CONTENTS

	Page
LIST OF TABLES	v
LIST OF FIGURES	vi
ABSTRACT	ix
1. INTRODUCTION	1
2. BACKGROUND AND RELATED WORK	4
2.1 Robotic Surgical Systems	4
2.2 Surgical Tools	6
2.3 Lumbar Discectomy Surgery	9
2.3.1 Open Discectomy	9
2.3.2 Micro-Endoscopic Discectomy	10
2.3.3 Arthroscopic Discectomy	11
2.4 Motivations	12
3. PROPOSED ROBOTIC SYSTEM	14
3.1 Design Requirements	14
3.1.1 Translational Motion	14
3.1.2 Rotational Motion	16
3.2 Design Details	17
3.2.1 Instrument Shaft Attachment	20
3.2.2 Translation System	20
3.2.3 Rotation System	21
4. PROTOTYPE FABRICATION	22
5. SYSTEM MODEL	26
5.1 Translational Motion	26
5.2 Rotational Motion	29
5.3 System Identification	30
5.4 Model Validation	37
6. CONTROL ALGORITHM DESIGN	40
6.1 Requirements	40
6.2 Position Tracking Controller Design	40
6.2.1 Translation	41
6.2.2 Rotation	42
6.3 Speed Tracking Controller Design	43

	Page
6.3.1 Translation	43
6.3.2 Rotation	44
6.4 Kalman Filter	45
7. SIMULATION	47
7.1 Translation System	47
7.2 Rotation System	51
8. EXPERIMENTAL RESULTS	56
8.1 Translation System	56
8.2 Rotation System	58
9. FUTURE WORK	62
10. CONCLUSIONS	64
REFERENCES	65

LIST OF TABLES

Table	Page
4.1 Electronic components.	24
5.1 System Parameters.	37

LIST OF FIGURES

Figure	Page
1.1 Normal Disc (Left) and Herniated Disc (Right) [2].	1
2.1 Intuitive surgical da Vinci Surgical System [8].	5
2.2 Overview of the throat surgical assistance slave [17].	6
2.3 Gear-train driven end-effector [18].	7
2.4 Cable driven end-effectors: MICA (Left) [19] and Force Bipolar with Du- alGrip (Right) [8]	7
2.5 Nerve Retractor (Left) and Grasper (Right) [20].	8
2.6 2-DOFs miniature manipulator being articulated [21].	9
2.7 5-DOFs Direct Drive Endoscopic System [22].	9
2.8 Open Discectomy [23].	10
2.9 MED procedure steps: A: Dilator insertion, B: Tubular retractors, C: Retractor with endoscope [24].	11
2.10 Arthroscopic microdiscectomy [25].	12
2.11 Robotic System from previous work [20].	13
3.1 Overview of the robotic lumbar discectomy system presented in [20]. The robotic cannula system allows for independent axial rotation and position- ing of instruments inserted into the instrument ports.	15
3.2 The cylindrical Workspace of the robotic cannula.	16
3.3 Free body diagram of the end-effector.	17

Figure	Page
3.4 (a) Overview of mechanical design of the robotic cannula system. The front cannula is inserted into the patient. The back cannula resides outside the patient. It has an outer housing (b) that covers the internal translation and rotation mechanisms (c). (d) Features are designed into the back of the housing to accommodate the motion constraints of the internal mechanisms. The instruments shafts are inserted and locked into the rack systems (e) that are driven by worm gears (f) to produce translational movement. Embedded motors and gears in the rack system (g) are used to produce rotational motion of the inserted instruments. An exploded view of the major components of the system is shown in (h).	19
4.1 Prototype robotic cannula system. The developed system can independently control the axial position and rotation of up to three surgical instruments.	22
4.2 Rack system.	23
4.3 Electronics and Microcontroller.	24
5.1 Force on the rack system.	28
5.2 Motor components.	31
5.3 The rise in the current.	32
5.4 Motor Voltage drop after power supply is shut down.	33
5.5 Calibration on the load cell.	34
5.6 Measurement of the motor constant.	35
5.7 Relationship between the armature current and the Back-EMF ratio. . . .	36
5.8 Translational position Response under sinusoidal reference.	38
5.9 Rotational position Response under sinusoidal reference.	39
7.1 Translational position tracking performance in ideal situation.	48
7.2 Translational position tracking performance in real situation.	49
7.3 Translational speed tracking performance in ideal situation.	50
7.4 Translational speed tracking performance in ideal situation.	51
7.5 Angular position tracking performance in ideal situation.	52
7.6 Angular position tracking performance in real situation.	53
7.7 Angular speed tracking performance in ideal situation.	54
7.8 Angular speed tracking performance in ideal situation.	55

Figure	Page
8.1 Position tracking performance in translational motion.	57
8.2 Speed tracking performance in translational motion.	57
8.3 Position tracking performance in rotational motion.	58
8.4 Speed tracking performance in rotational motion.	59
8.5 Stepping up and down in position tracking for the translational and rotational system when Kalman filter is not applied.	60
9.1 Future add-on design to enable the rotation of the Robotic Cannula system.	62

ABSTRACT

Ding, Yang MSME, Purdue University, August 2019. Design of a Robotic cannula for Robotic Lumbar Discectomy. Major Professor: David J. Cappelleri, School of Mechanical Engineering.

In this thesis, the design of the robotic cannula for minimally invasive robotic lumbar discectomy is presented. Lumbar discectomy is the surgery to remove the herniated disc material that is pressing on a nerve root or spinal cord.

Recently, a robotic approach to performing this procedure has been proposed that utilizes multiple teleoperated articulated instruments inserted into the surgical workspace using a single cannula. In this paper, a new robotic cannula system to work in conjunction with this new procedure is presented. It allows for the independent teleoperated control of the axial position and rotation of up to three surgical instruments at the same time. The mechanical design, modeling, controller design, and the performance of the prototype of the new system are presented in this paper demonstrating a fully functioning device for this application. A novel worm gear and rack system allow for the instrument translation while an embedded gear train produces the rotational movement. Steady-state errors of less than $10\text{ }\mu\text{m}$ for translation and less than 0.5° for rotation motion are achieved in position tracking; steady-state errors of less than $100\text{ }\mu\text{m/sec}$ of translation and less than $0.5^\circ/\text{sec}$ for rotation motion are obtained in speed tracking.

1. INTRODUCTION

Back pain is a common condition encountered by 75% to 85% of all Americans during their lifetime [1]. A common cause is typically a herniated disc, shown in (Fig.1.1), in the spine.

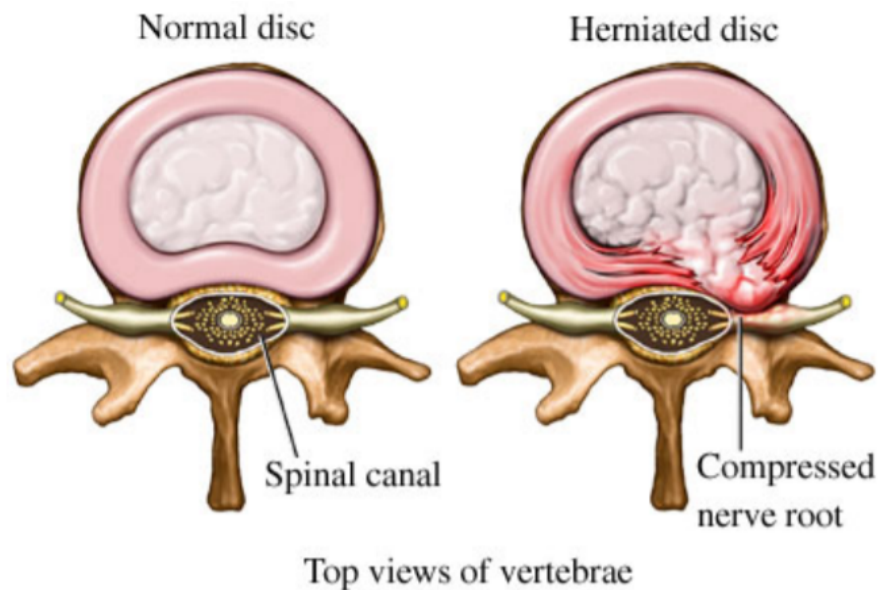


Figure 1.1. Normal Disc (Left) and Herniated Disc (Right) [2].

The disc is an elastic ring made of soft material that resides between and provides cushion to the vertebral bones. When the elastic ring gets weakened, the soft material will herniate and protrude from the boundary of the spine and compress the nerves in the spinal column.

To cure this condition, rest, medication and physical therapy are often prescribed. However, many times surgery is required to remove the herniation. This type of procedure is called lumbar discectomy. More than 300,000 cases each year of it are performed in the United States [3]. During this surgery, part of the damaged disc is

removed and taken out of patient's body to release the pressure on the spinal cord and nerves and therefore ease the pain. Open laminotomy and laminectomy procedures, which involve large incisions and longer recovery times, have traditionally been used to treat disc herniation. Recently, minimally invasive surgery (MIS) prospers with the advancement of the technology in surgery, and minimally invasive procedures for lumbar discectomy have thus emerged resulting in smaller incisions, through which the endoscope, the stereo vision and surgical tools are inserted into the human body, and thus discomfort, healing time, and risk of infection are reduced for patients [4].

However, the difficulties involved in operation of the surgical tools through such a small hole demand high-skill surgeons. One of the most challenging tasks for the surgeon during the MIS is to orient and align the surgical tools, which do not possess a high dexterity of operation. The frequent realignment and readjustment in the orientation increase the chance of hurting the soft tissue in the human body. The smaller the incision, the more difficult it is for a surgeon to perform MIS as the work space is extremely limited. In addition, the long and rigid instrument shaft used in the spinal surgery tends to amplify the tremor produced from the surgeon's hands as the insertion point acts like a rotation pivot [5].

Robotic surgical system therefore is designed and introduced to help improve on the minimal invasive surgery in many ways. The positioning and orientation of the surgical tool hold by a robotic arm is much more precise and robust than a human hand even of a very experienced surgeon, who may feel tired after hours of operation. In some case of a toxic environment, robotic surgical system is the first choice to replace the physician. There are many industrial level robotic surgical system, among which MINOSC and da Vinci system are most well known in the case of endoscopic spinal surgery.

However, these devices are very expensive and space occupying while not yet targeting all kinds of operations. In terms of curing the herniated disc, such expensive and complex systems require a very experienced surgeon to operate, and thus the price would be too high for the patients to pay for the little pain on their back.

The maintenance of these robotic surgical system is also costly and requires a good engineer or technician, while there is still the risk of malfunctioning.

Thus there is a call for a new device, which should be cheaper, smaller and easier to operate, specifically targeting at some minimally invasive procedures such like the lumbar discectomy so that the patients suffering from this disease will be more willing to accept the MIS rather than resting and holding the pain for their whole life. The main objective is to design a robotic surgical system specifically for the minimally invasive lumbar discectomy and other similar procedures without compromising the surgery quality, and such a robotic surgical system is proposed in this thesis.

In Chapter 2, the background of minimally invasive surgery, existing surgical techniques and tools for the lumbar discectomy are discussed. The mechanical structure and mechanism of the proposed device is discussed in Chapter 3. Chapter 4 aims to lead the reader through the manufacturing and assembly of the prototype, and the components of the device are listed there. Chapter 5 involves the mathematical model of the device in terms of the translation as well as rotation parts. Then the control algorithms for the translational as well as rotational position and speed tracking of the instrument shaft are designed and discussed in Chapter 6. In Chapter 7, the simulation results, position tracking and speed tracking response, of the translation system and rotation system are provided and discussed. Chapter 8 covers the experimental results of the tracking. Some future work is discussed in Chapter 9.

2. BACKGROUND AND RELATED WORK

2.1 Robotic Surgical Systems

Robot has many advantages including the precise positioning, stable maneuver as well as the capability working in extreme conditions like low temperature or toxic environments [6]. Thus diverse of robotic systems for surgery emerge on the market aiming to assist in the surgery. These devices are designed to assist the surgeons to perform different tasks during surgery including preoperative planning, intraoperative registration to presurgical plans, use of robotic assist and manually controlled tools to carry out the plan, and postoperative verification and follow-up [7]. According to the authors of [7], surgical robots can be splitted into two main categories: *surgical computer-aided design/manufacturing system (CAD/CAM) systems* and *surgical assistants*. The first class device aims to automatically generate passable path within the human body using the available 3D data achieved from the data acquisition stage, during which imaging techniques are applied including but not limiting to CT/MR and X-ray. The second class can be further broken down into two subclass: *surgical extendors* and *auxillary surgical supports*. *surgical extendors* is purely an extension of the surgeons hands and to be operated directly by the surgeons; while *auxillary surgical supports* is more like a support to the surgeon, holding some auxillary equipment like endoscope.

Examples of some robotic system for surgery include the MINOSC (micro-neuro endoscope) [9], the Mazor Robotics Renaissance Guidance System [10], the Globus Medical ExcelsiusGPS Robotic Navigation system [11], and the Intuitive Surgical da Vinci surgical system [8]. The MINOSC is a smart endoscope that uses real-time image processing techniques to provide the surgeon with direct vision of the surrounding structures in the spine but cannot perform any surgical operations itself. Similarly,



Figure 2.1. Intuitive surgical da Vinci Surgical System [8].

the Renaissance and ExcelsiusGPS systems are robotic guidance systems for pre-operative and intraoperative planning of tool insertion trajectories and thus, they cannot perform surgery procedures without the use of additional instruments. The da Vinci system shown in (Fig.2.1) is a teleoperated system consisting of multiple, rigid surgical manipulators and a 3D endoscope. It was used with prototype instruments for laminotomy, laminectomy, disc incision, and dural suturing procedures in [12], parabertebral tumor resections in [13], transoral decompression of craniocervical junction in [14], and anterior lumbar interbody fusion in [15]. With this system, the surgeons are now able to get access to the inside of human body through the tiny insertion without losing dexterity. However, due to the systems size and limited force capabilities, the da Vinci is not suitable for disc herniation procedures.

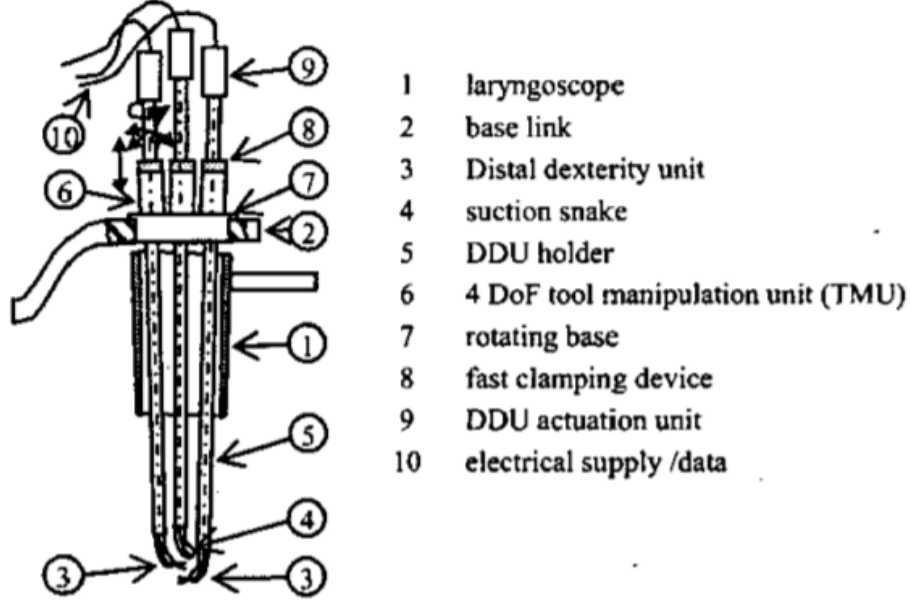


Figure 2.2. Overview of the throat surgical assistance slave [17].

There are some other smaller systems in the research areas. The device introduced in [16] is used for colonoscopy, and the working principle is propulsion mechanism based on the inchworm locomotion. In [17], a high-dexterity robotic system, shown in (Fig.2.2), for minimally invasive surgery (MIS) of the throat is developed. The distal dexterity units, or DDU are hold by the DDU holder, and they provide a high dexterity in the procedure to bypass the obstacle. Rotation motion is also provided on the base. The whole system can perform very complicated surgery while the system itself is also very complex, consisting of 34 actuators and many more tiny parts.

2.2 Surgical Tools

To better accommodate the robotic system for surgery, robotic surgical manipulators and tools have been designed in the research community. A large size and heavy duty gear-train driven mechanism for dexterous placement of an end-effector during minimally invasive surgery [18] is shown in Fig 2.3.

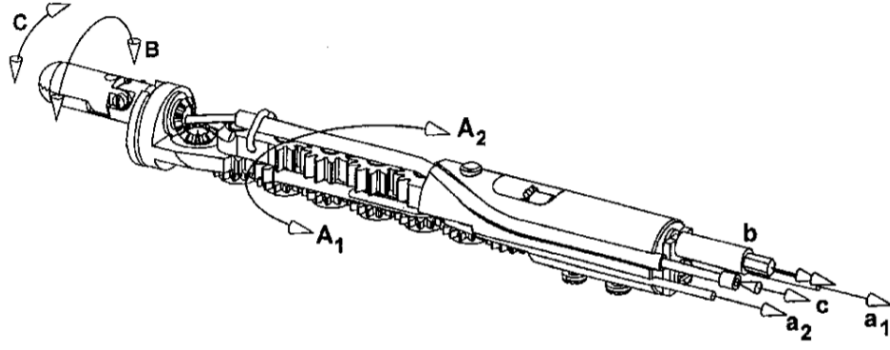


Figure 2.3. Gear-train driven end-effector [18].



(a) MICA



(b) Force Bipolar with DualGrip

Figure 2.4. Cable driven end-effectors: MICA (Left) [19] and Force Bipolar with DualGrip (Right) [8]

This kind of actuation is not so popular at current stage in the MIS due to its large size and lack of dexterity. Instead, nowadays the tendon or cable driven rigid robotic end-effectors are most popular because of the small size, high dexterity and powerful actuation core located at the base of the robot. Two examples are given in (Fig.2.4(a)) and (Fig.2.4(b)). The MICA in (Fig.2.4(a)) is a versatile instrument for minimally invasive robotic surgery. Being a 3DoF-robot, it is attached to the MIRO arm and extends the kinematic chain by three joints. In 2010 the MICA was presented

to the public for the first time [19]. The Force Bipolar with DualGrip developed by Intuitive is also cable driven and is a 3Dof-robot.

Besides the above commercialized end-effectors, the end-effector developed in [20] also possesses high dexterity. (Fig.2.5) shows two types of the end-effectors, which are both manufactured using 3D printer and actuated using cable in yellow color. The black portion is the flexible link made from a soft material that can be bend. When the cable is pulled, the nerve retractor can be articulated, and the grasper can orient and grasp.

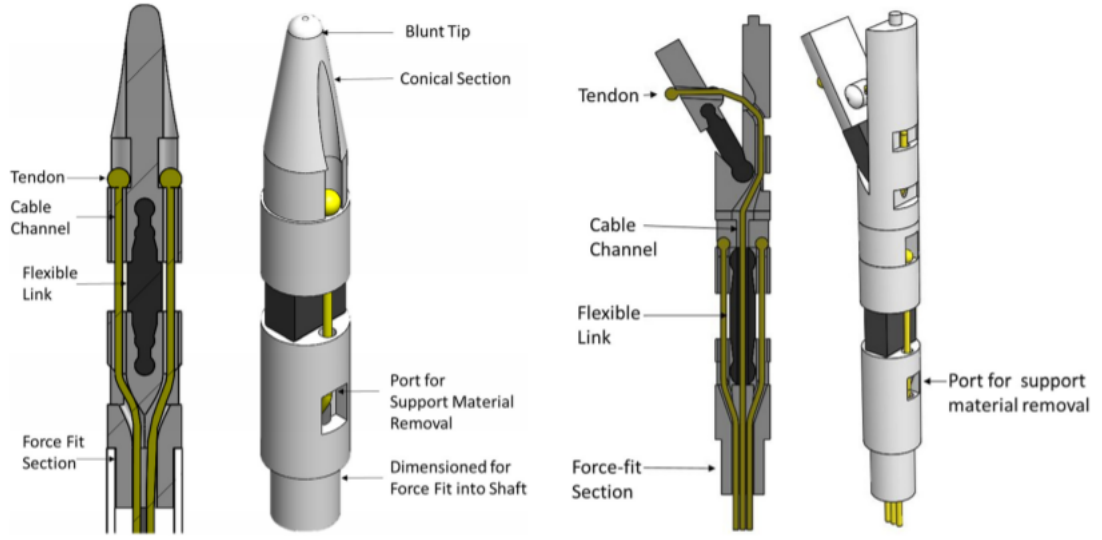


Figure 2.5. Nerve Retractor (Left) and Grasper (Right) [20].

There are many other high-dexterity end-effectors being developed. In [21], a 2-DOFs miniature manipulator of 3.5-mm diameter and tips bending part manipulated by independent motions is introduced, and it is shown in Fig. 2.6.

In [22], a Direct Drive Endoscopic System is introduced. It is a 5-DOFs device and it can perform very complex task such like tying sutures as well as providing traction and counter traction, and it is shown in Fig. 2.7.

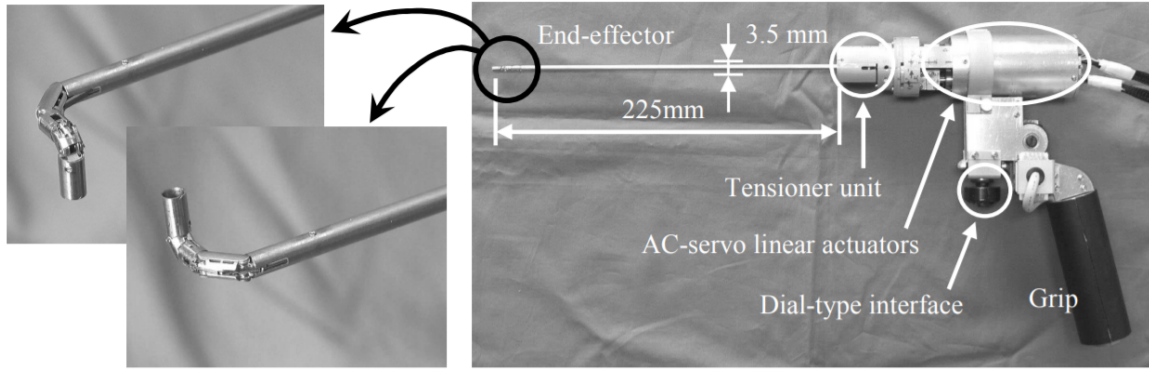


Figure 2.6. 2-DOFs miniature manipulator being articulated [21].



Figure 2.7. 5-DOFs Direct Drive Endoscopic System [22].

2.3 Lumbar Discectomy Surgery

2.3.1 Open Discectomy

Open discectomy is a traditional surgical treatment to the herniated disc. The setup of this type of surgery is shown in (Fig.2.8) To remove the fragment of the herniated disc, an incision about 3 centimeters in length is made on the patient's

back. Then the muscles are dissected away from the bone of the spine. A small amount of bone and ligament from the back of the spine is removed afterward to let see the herniated disc. Then the surgeon use the surgical tools to remove the disc materials, and the incision is closed with a bandage applied once finished.

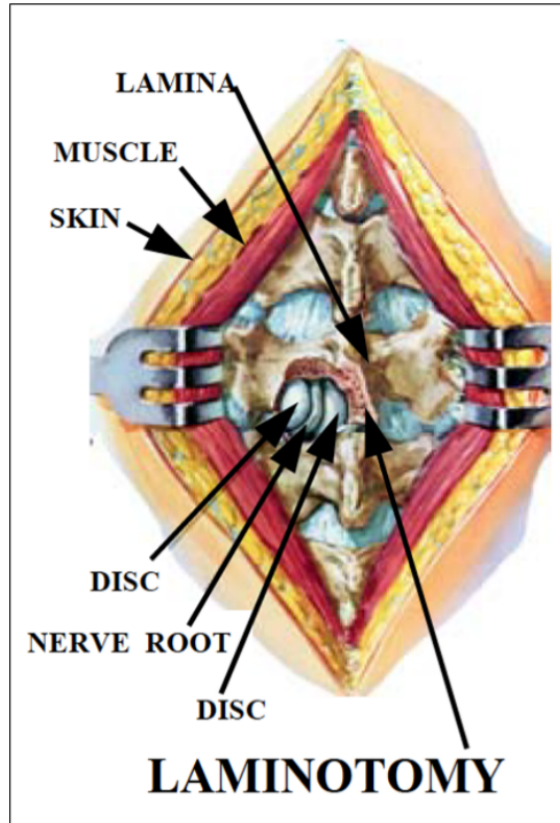


Figure 2.8. Open Discectomy [23].

2.3.2 Micro-Endoscopic Discectomy

In MED, a needle is placed into the patient and guided fluoroscopically to the desired position in the patient as shown in (Fig.2.9. Once it is in position, the needle is replaced with retractors. These retractors are docked to the bone of the spinal

column and other instruments inserted through them to gain access to the surgical workspace, all through about a 25 mm long incision.

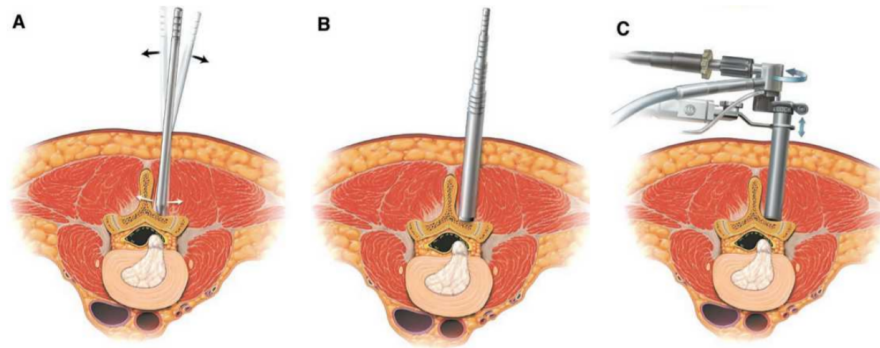


Figure 2.9. MED procedure steps: A: Dilator insertion, B: Tubular retractors, C: Retractor with endoscope [24].

The instruments used in this procedure typically include a fixed endoscope (camera) and manually controlled rigid tools.

In MED, the endoscope is fixed into position in the retractor and thus the surgeon must move the retractor around to re-position the endoscope to obtain is optimal position. This process can lead to tissue trauma for the patient.

2.3.3 Arthroscopic Discectomy

AMD surgery can be performed using one or two ports requiring 1 cm skin incisions each. An endoscope is inserted through one port while other instruments are inserted through the other port.

In this surgical technique, the protective bone and ligaments over the posterior surface of the vertebral canal are not pierced as in the case of MED. Instead, small tubes, called cannulas, are passed through the skin and muscle layers through the right and left side of the patient. The surgeon is able to position the cannula(s) directly under the outer layer of the annulus of the disc and the posterior longitudinal ligament, guided by fluoroscopy or an endoscope. From here, the herniation is

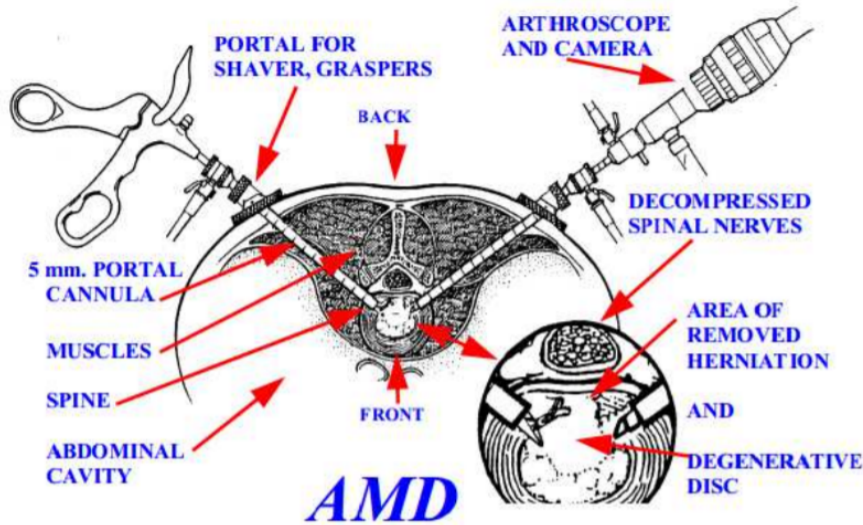


Figure 2.10. Arthroscopic microdiscectomy [25].

removed using a combination of rigid tools and irrigation/suction instruments, with or without the help of the endoscope.

For the workspace when performing AMD, the vision and dexterity provided to the surgeon is extremely limited. The nature of the size and capabilities of tools being used can also force blind operations at times in order to access the herniated disk material. This can increase the risk of complications.

2.4 Motivations

As mentioned in the introduction chapter and discussed in this chapter, the disc herniation results in back pain and lumbar discectomy is often applied to cure the condition. But all the lumbar discectomy methods do not involve the robotic system and current robotic systems on the market cannot perform lumbar discectomy.

In the previous work of MSRAL, a robotic system shown in (Fig.2.11) is specifically designed for the lumbar discectomy to resolve the problem. The instrument shaft is mounted on the system, which provides translation motion using stepper motor and

rotation motion using servo motor. The pulleys driven by servo motors are used to manipulate the end-effector. Together, these actuators can provide the same actions as operated by a surgeon: twisting and pulling on the herniated disc. However, this system is too large for multiple tools to be operated at the same time.

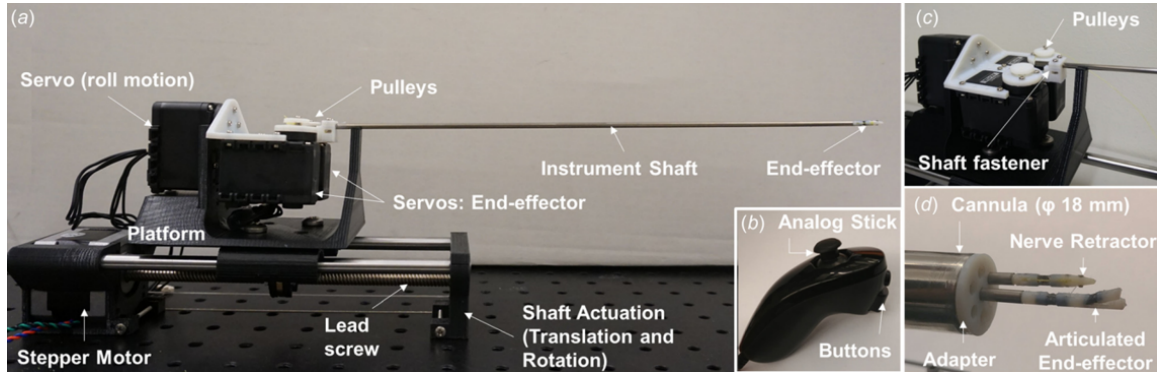


Figure 2.11. Robotic System from previous work [20].

Thus there is a call for a new system, which should be smaller, allow multiple surgical tools to be used at the same time and specifically target at lumbar discectomy. The main motivation is to design a robotic surgical system specifically for the minimally invasive lumbar discectomy and such a robotic surgical system is proposed in this thesis.

3. PROPOSED ROBOTIC SYSTEM

In this chapter, the design of the surgical system in terms of mechanical parts and control algorithm are presented. The design requirements are introduced, and the details in design are discussed.

3.1 Design Requirements

(Fig.3.1) shows a schematic of the robotic cannula. The diameter of the cannula inserted into patient's body should be less than 1 inch, and the design of the device should make it possible to load most of the current surgical tools. The surgical tools inserted into the robotic cannula should be able to rotate and translate independently of each other with the teleoperated control. That is, when one of the instruments is moved axially along the motion axis, it should not affect the motion of the other instruments. The articulation on the surgical tool should also be independent from the translation and rotation motion. In addition, the robotic cannula should be able to manipulate 3 to 5 tools at the same time. Furthermore, the motion of the tools needs to be precise enough to prevent any misalignment or unexpected movement in patient body. The surgical tool needs to be inserted into the system and into the patients body, and the tool should be detachable after the procedure while stay fixed on the system during the surgery. In the following sections, the detailed design requirements for both the mechanical system and the control system for the robotic cannula will be discussed.

3.1.1 Translational Motion

The work space of the spine for performing lumbar discectomy is approximately a 1 cm^3 cube. Thus, the translation range for instruments inserted into the robotic

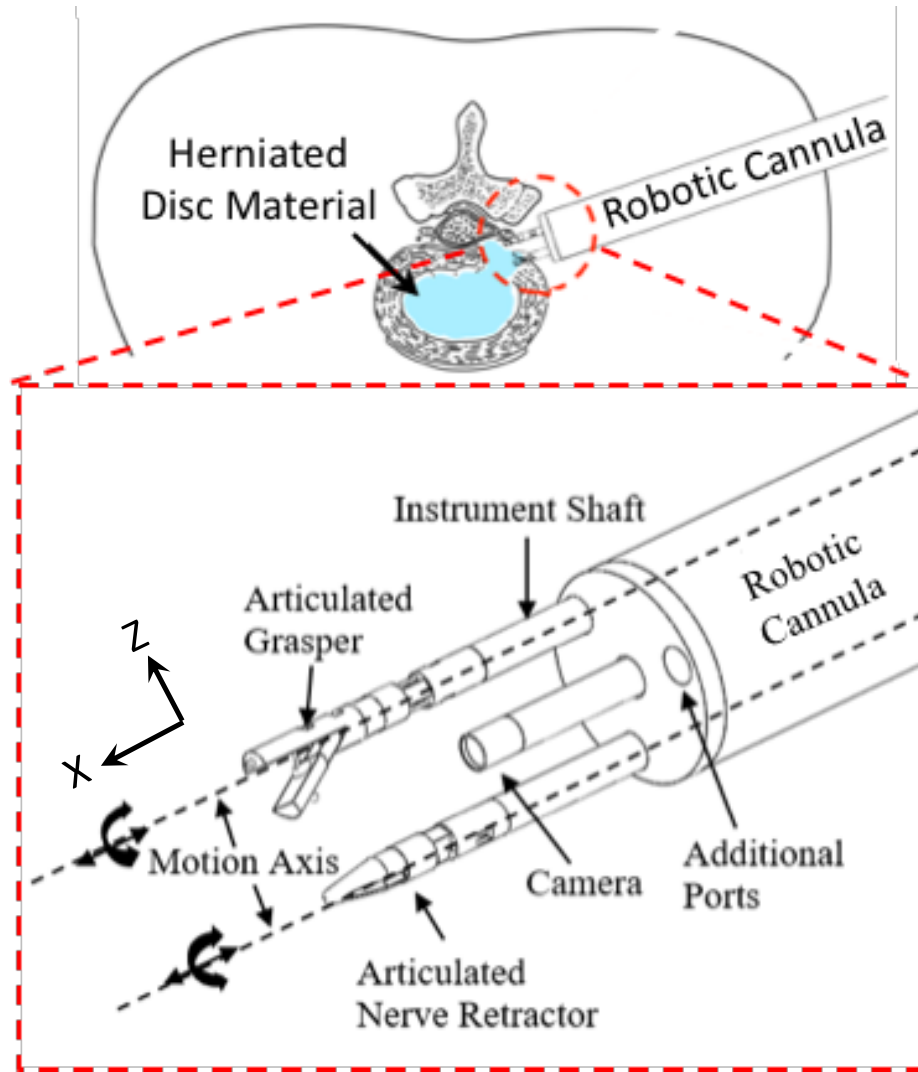


Figure 3.1. Overview of the robotic lumbar discectomy system presented in [20]. The robotic cannula system allows for independent axial rotation and positioning of instruments inserted into the instrument ports.

cannula is designed to be $10\text{ mm} (\pm 5\text{ mm})$ with a minimum incremental motion requirement of 0.5 mm . During the surgery, the tendon wires in the instrument shaft are actuated to manipulate the end-effectors. In the case of the nerve retractor end-effector, it is deduced in [20] that the maximum retraction force required for the procedure is 0.35 N . Therefore the translation subsystem should be robust and sturdy enough to hold withstand a force of 0.60 N in magnitude [26].

3.1.2 Rotational Motion

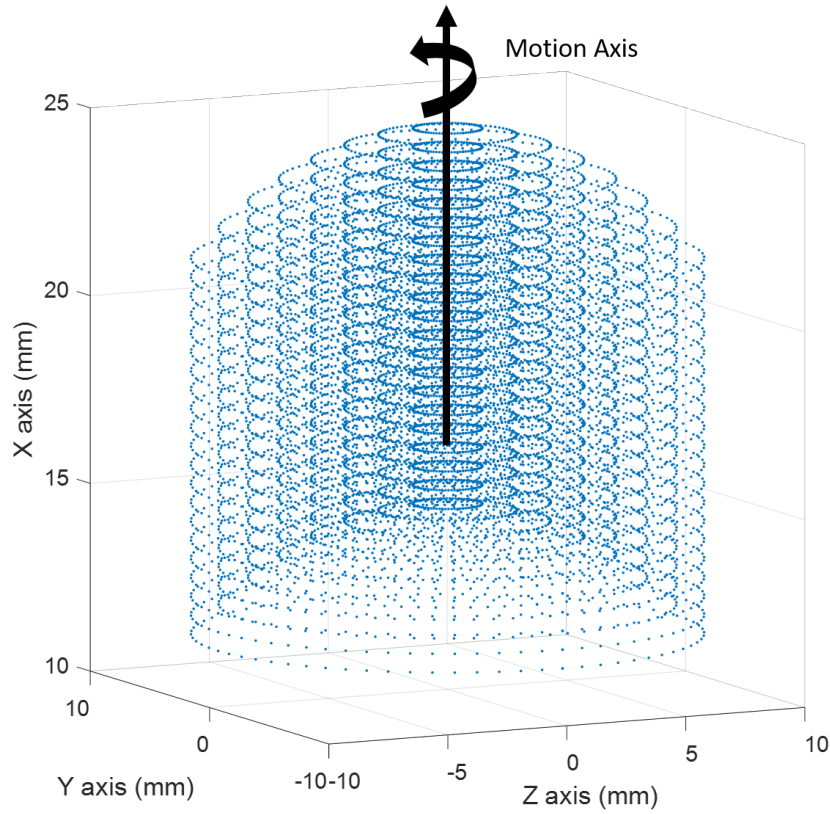


Figure 3.2. The cylindrical Workspace of the robotic cannula.

The designed instrument end-effectors can be articulated in two directions by actuating the appropriate tendon wire. Therefore 180° of rotation of the instrument shaft is enough for the end-effector to reach every point in a cylindrical workspace, as shown in (Fig.3.2).

The minimum incremental motion for rotation is set at 5° . In the free body diagram shown in (Fig.3.3), the maximum torque applied on the instrument shaft can be calculated. F_y is the maximum force of 0.35 N acting on the tip of the end-effector in the direction of Y axis. The length of ac is 1.5 cm and thus ab is 0.964

cm given the maximum angle is 40 degrees. Therefore, the maximum torque on the instrument shaft is $0.337\text{ N} \cdot cm$.

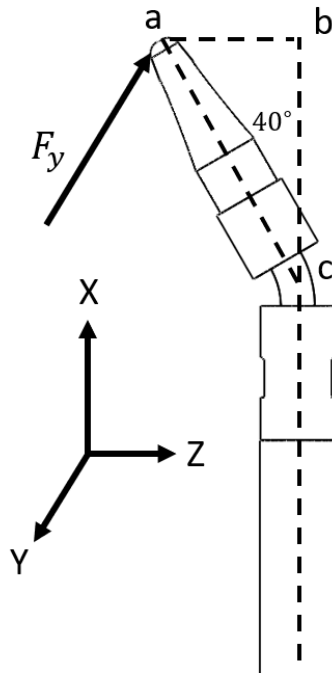


Figure 3.3. Free body diagram of the end-effector.

3.2 Design Details

A new robotic lumbar discectomy (RLD) surgical system is proposed. The procedure requires a cannula to introduce tools into the surgical workspace. The cannula is fixed outside the body and does not rigidly attach to any anatomy. However, it is designed to accommodate multiple surgical tools at a time that can work together that are teleoperated by a surgeon, as shown in (Fig.3.1). An endoscopic camera and irrigation system, used to clear the workspace, can also be inserted through the cannula into the surgical workspace. To ensure a low-cost system and eliminate the need to sterilize the instruments between uses, the surgical instruments are designed to be disposable. The design and evaluation of two different disposable robotic surgical

instruments (articulated nerve retractor and grasper) for use in the proposed system were described in [20]. Each has an identical instrument shaft with 3D printed mechanism inserts driven by tendon wires that are teleoperated by the surgeon. It is desired to be able to independently robotically control the axial rotation and position of the instruments inserted into the cannula system for dexterous operation in the surgical workspace. Therefore, in this thesis presents the design of a robotic cannula that can accommodate multiple different instruments and independently control their axial rotation and translation in the workspace of the spine.

The overall mechanical design of the robotic cannula system is shown in (Fig.3.4). The sub-figures show different views of the major components of the system; these major components are labelled numerically. The operation of the mechanical system and system components of this figure will be described now.

The cannula consists of a front and back portion, as shown in (Fig.3.4(a)). The front portion is the part that is inserted into the patient. It has a diameter of approximately 19 mm, ensuring a minimally invasive incision (i.e., <1"). The back portion of the cannula has a diameter of 60 mm, is 127 mm in length, and is designed to be rigidly mounted outside of the patient. The instrument ports are 4 mm in diameter to allow for our custom instruments as well as existing laparoscopic tools to be used with the system. The instruments are inserted from the rear of the back portion of cannula and extend all the way through the front cannula and into the surgical workspace where the surgeon can teleoperate them to perform the procedure.

(Fig.3.4(b)) shows the outside housing of the back cannula. The circular cutout (1) is used to couple it to the front cannula. The holes (2) are for the instrument shafts inserted into the system. (Fig.3.4(c)) shows the overview of the internal mechanical structure of the robotic cannula system, located in the back cannula. The housing of the back cannula slides over internal mechanisms and latches in place using the friction slots (3). This system can independently control up to three instruments. Each instrument is controlled with a rack system (4). Once inserted into the cannula, the instrument shaft is attached to the rack system. The rack system will rotate the

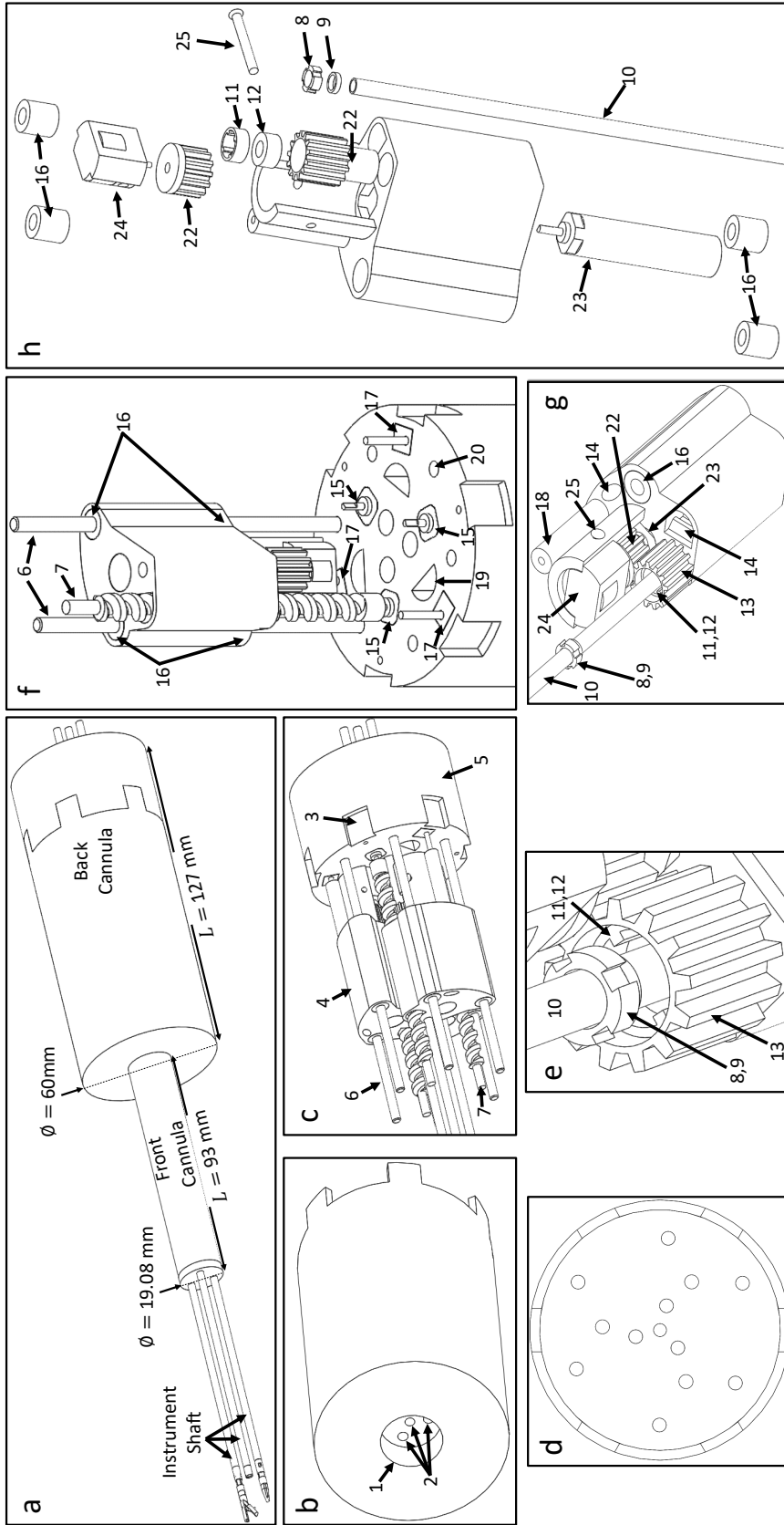


Figure 3.4. (a) Overview of mechanical design of the robotic cannula system. The front cannula is inserted into the patient. The back cannula resides outside the patient. It has an outer housing (b) that covers the internal translation and rotation mechanisms (c). (d) Features are designed into the back of the housing to accommodate the motion constraints of the internal mechanisms. The instrument shafts are inserted and locked into the rack systems (e) that are driven by worm gears (f) to produce translational movement. Embedded motors and gears in the rack system (g) are used to produce rotational motion of the inserted instruments. An exploded view of the major components of the system is shown in (h).

instrument shaft and the base system (5) will translate the rack system together with the instrument shaft along the motion axis. (Fig.3.4(d)) shows the other end of the housing shown in (Fig.3.4(b)) that has holes to constrain the linear shafts (6) and worm gears (7) that are part of the translation system. In the following sections, the details on the mechanical design of the instrument shaft attachment system, the translational motion, and rotational motion systems will be presented.

3.2.1 Instrument Shaft Attachment

As seen in (Fig.3.4(e)), a locking collar (8) and ring magnet (9) are glued to the instrument shaft (10) to make it compatible with the robotic cannula system.

The mounting location for these depends on the length of the instrument shaft. There is another locking collar (11) and ring magnet (12) mounted to the gear (13) of the rack system. When the instrument shaft is inserted into the robotic cannula, it will go through the center of the gear (13). Thus, the two magnets are attracted and attach to each other and are prevented from rotating relative to each other by the two locking collars. The instrument shaft will only rotate when the gear (13) is driven by the rack system and only translate when actuated by the base system. The attraction force between the magnets when they are attached is calculated to be about 0.80N. This is greater than the 0.60N force requirement. Thus the instrument shaft can be securely fixed on the rack system during the procedure. The force value is also low enough so that after the procedure, the instrument shaft can be manually disengaged from the locking mechanism in the gear and removed from the cannula.

3.2.2 Translation System

(Fig.3.4(f)) is an isolated view of one of the three rack systems shown in (Fig.3.4(c)) to more clearly illustrate the translation mechanism. The translation is realized through the use of a worm gear (7) and the rack system (4). (Fig.3.4(g)) shows a close-up of the rack system for one particular instrument. It is the underside view

of the rack shown in (Fig.3.4(f)). The worm gear rotates on the internal rack, that can be seen through the slot (14). The motor (15) is attached to the worm gear. Therefore, when the motor spins, the rack system will move along the shafts (6). To smooth the movement, four sleeve bearings (16) are fixed in the rack system. The ratio between the worm gear rotation and the rack system translation is 1:5 rev/mm. That is, the rack system will move 5mm along the motion axis for a single revolution of the worm gear, and thus, so will the instrument shaft.

In addition to these mechanical parts, a linear motion potentiometer (17) is embedded into the base. Its shaft is fixed to the rack system at the location indicated as (18). The holes (19) on the base system are used for wire routing of rack systems sensors and motors; the holes (20) are used for mounting the linear shafts (6); the three holes (21) in the middle are for the instrument shafts.

3.2.3 Rotation System

There is a pair of gears on the rack system as indicated in (Fig.3.4(g)). The gear (22) is attached to a motor and the other gear (13) is locked to the instrument shaft. The gear ratio between these two gears is 1:1. Therefore, when the rack motor (23) spins, the instrument shaft will rotate in the opposite direction at the same angular speed. The maximum torque at the motor shaft is $8.82N \cdot cm$. Both gears have a diameter of $8mm$, and thus the torque on the instrument shaft will be about $11N \cdot cm$, which is far more than the torque requirement.

To measure the rotation of the shaft, a rotary potentiometer (24) is used. It is fixed on the rack system using a 1.5mm bolt (25). The shaft of the potentiometer is coupled with the gear (22) so it can directly read the rotation amount of the instrument.

An exploded view of the major components of the rack system is shown in (Fig.3.4(h)).

4. PROTOTYPE FABRICATION

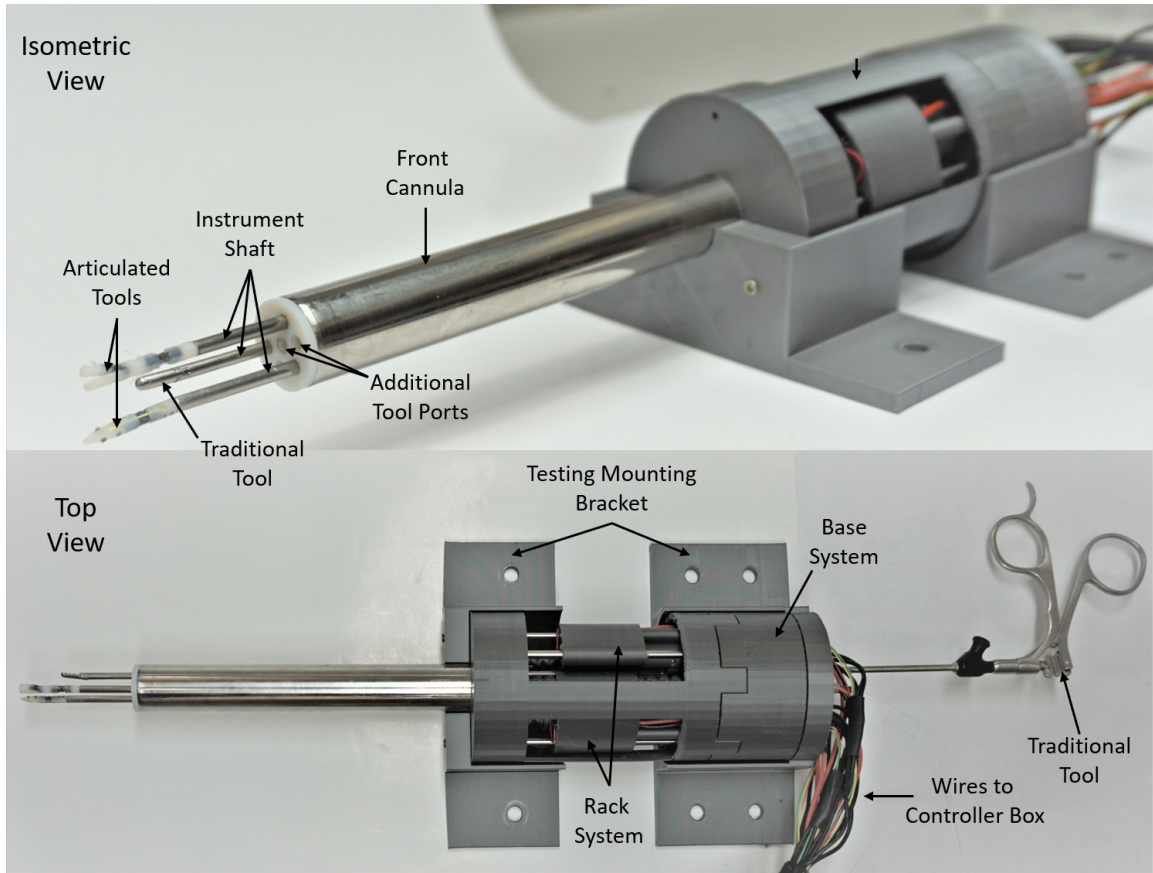


Figure 4.1. Prototype robotic cannula system. The developed system can independently control the axial position and rotation of up to three surgical instruments.

A prototype robotic cannula system was fabricated, as shown in (Fig.4.1). A more detailed view on the rack system is given in (Fig.4.2) at the end of this chapter.

For this proof-of-concept design, the prototype was constructed from off the shelf hardware and 3D printed components. Instruments developed from our previous work as well as an existing laparoscopic surgical instrument were inserted into to for

validation testing, as described in the next section. The back cannula is intentionally printed open for test and demonstration purposes. Also, for convenience in testing, the system is mounted horizontally using custom mounting brackets. In the real application, the device will be mounted vertically above the patient.

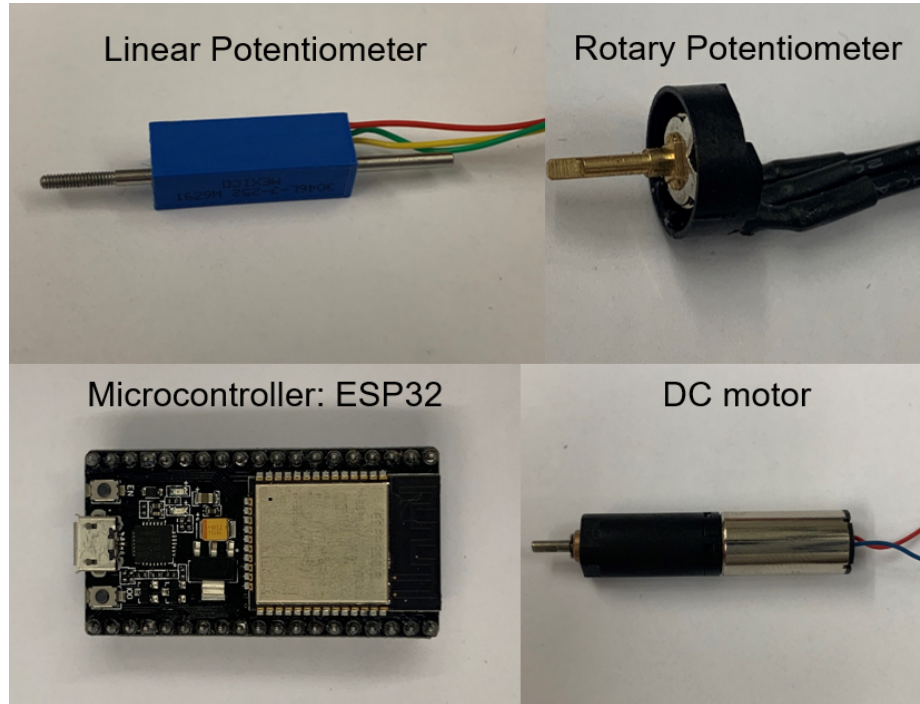


Figure 4.3. Electronics and Microcontroller.

Table 4.1. Electronic components.

Part Name	Manufacturer	Part Number
Linear Potentiometer (17)	Bourns	3046L-3-252
Rotary Potentiometer (24)	HobbyKing	HXT900
Motor (9,23)	ZhaoWei	ZWPD008008-47
ESP32 Microcontroller	Espressif Systems	3-01-1287
L289N Motor Driver	Qunqi	MK-050

The front cannula tube, linear shafts, sleeve bearings, and mounting hardware was sourced from McMaster Carr while the ring magnets were obtained from SuperMagnetMan. Table 4.1 lists the key electronic components of the system and they are shown in (Fig.4.3). The linear potentiometer used has a range of 12.7 mm ($\pm 6.35\text{ mm}$); the rotary potentiometer has a range of 180° ($\pm 90^\circ$). (Note: the rotary potentiometers were harvested from a HobbyKing HXT900 servo motor, part number HXT900) Since both potentiometers are analog sensors, the resolution of the measurement depends on the ADC chip on the chosen microcontroller. The ESP32 microcontroller from Espressif Systems with a 12-bit analog to digital converter was selected for use here. Therefore, it can provide a resolution of $3.1\text{ }\mu\text{m}$ and 0.044° for translation position and rotation angle sensing, respectively. The same motors are used to drive the worm gear in the base system and the gear train in the rack system from Shenzhen ZhaoWei Machinery & Electronics Co. Ltd. The motor driver used is a standard L298N H-bridge. All the remaining custom designed parts were 3D printed out of PLA filament material.

The system may potentially fail due to various reasons. The first failure mode is from the instrument locking mechanism shown in (Fig.4.2). The rotation lock is glued on the instrument shaft using a strong glue, of which the strength will decay with time and if being heated or reacted with chemicals. When the glue's strength is gone, the rotation lock will detach from the instrument shaft, which will then be free of constraints and potentially hurt the patients during the procedure. In addition to the mode described above, the failing will occur on the moving parts like gears. Gears made of PLA material are not as hard and strong as metal like stainless steel, and deformation will occur on the gear when it is coupled with the shaft of the motor. When the plastic deformation happens, the gear will be permanently damaged and thus decoupled with the motor shaft. Finally, the motor itself can fail in the procedure. The gearbox of the motor consists of many plastic gears, which will be damaged if being stalled for a long period.

5. SYSTEM MODEL

Due to the mechanical structure discrepancy, the models of translational system and rotational system are different though these two systems use the actuator of same dynamics. In this section, both models are derived in details.

5.1 Translational Motion

The current of the winding on the rotor has a first order dynamics given in Equation (5.1) [27].

$$L \frac{d}{dt} i_a + R i_a = u - K_b \dot{\theta}_a \quad (5.1)$$

i_a is the current in the winding; L is the inductance of the motor; R is the resistance of the motor; u is the voltage supply to the motore; K_b is the back-EMF constant; $\dot{\theta}_a$ is the angular speed of the rotor. The rotor angular speed has the dynamics in Equation (5.2) [27].

$$J_t \ddot{\theta}_a + b \dot{\theta}_a = T_a - T_L - \frac{1}{n_1} T_f \quad (5.2)$$

$J_t = J_a + J_g + \frac{1}{n_1^2} J_w$ is the total inertia; J_a is the rotor inertia, J_g is the inertia of the gear box and J_w is the ineria of the worm gear. b is the viscous friction coefficient of the motor; T_a is the torque generated by the rotor, and the toque is proportional to the current: $T_a = K_t i_a$. K_t is the current to toque constant of the motor. T_f is the frictional torque in the worm gear system and n_1 is the gear ratio of the gear box. T_L is the external load mounting to the rotor shaft. In the case of translational motion, the external load comes from the rack system, which has the dynamics in Equation (5.3). Note that during this development stage, the system is tested when placed horizontally, and thus gravity is not considered.

$$m\ddot{y} = F - F_{ct} - d(t) \quad (5.3)$$

m is the total mass of the rack system. y is the displacement of the rack system. F_{ct} is the Coulomb Friction along the motion axis, and it can be written as $A_{ct} \cdot \text{sgn}(\dot{y})$. $d(t)$ is the arbitrary bounded disturbance along the motion axis during the operation. F is the force along the motion axis applied on the rack system by the worm gear.

(Fig.5.1) illustrates the force on the rack system. F is in the direction of the red arrow when the worm gear rotates clockwise. Assume $F = \gamma T_{LS}$, in which $T_{LS} = n_1 T_L$ is the load on the motor shaft directly connected to worm gear and n_1 is the gear ratio of the gearbox. F_t and F_n is the tangential force and normal force exerted by worm gear on the rack pitch surface. Ideally, Tangential force F_t has the same magnitude of the friction between the worm gear and rack. Thus, $F_n = \frac{F_t}{C_f}$, where C_f is the friction coefficient. F_n has a component $F = F_n \cos(\phi_p)$. Lastly, T_{LS} is due to the friction between the worm gear and the rack. Assuming perfect contact without backlash, $T_{LS} = F_t L_E$, where L_E is the effective length for the torque. Combining the relations above, F and T_L can be related using Equation (5.4). Apparently, γ is a small number since the denominator is much larger than the numerator. Thus it can be infer that the external disturbance and the Coulomb friction along the motion axis will not bring much disturbing effect to the system.

$$T_L = \frac{C_f L_E}{n_1 \cos(\phi_p)} F = \gamma F \quad (5.4)$$

Combine Equation (5.2), Equation (5.3) and Equation (5.4), Equation (5.5) can be achieved. From this equation, it can be observed that the load of the system comes from the friction, disturbance and the inertia force of the rack system.

$$J_t \ddot{\theta}_a + b \dot{\theta}_a = K_t i_a - \gamma (m \ddot{x} + F_{ct} + d(t)) - \frac{1}{n_1} T_f \quad (5.5)$$

$$\theta_a = n_1 \theta_s \quad (5.6)$$

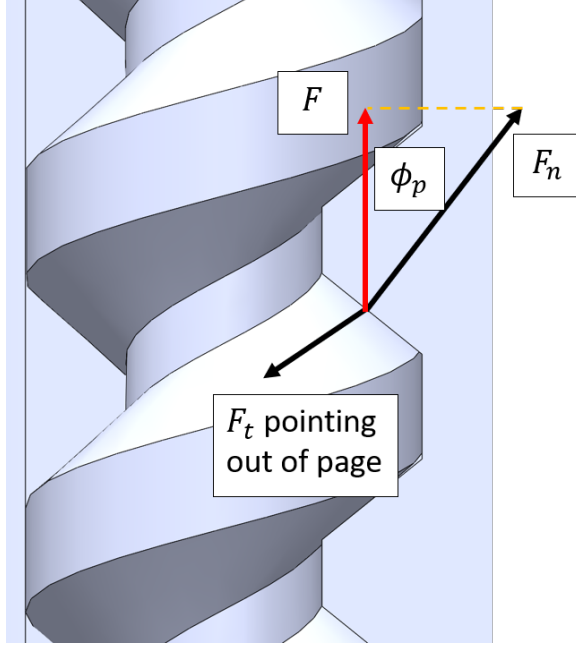


Figure 5.1. Force on the rack system.

$$\theta_s = n_2 y \quad (5.7)$$

The kinematics relations given in Equation (5.6) and Equation (5.7) help to further change Equation (5.5) to Equation (5.8). Equation (5.1) can be modified to Equation (5.9).

$$(J_t n_1 n_2 + \gamma m) \ddot{y} + b n_1 n_2 \dot{y} = K_t i_a - \gamma F_{ct} - \gamma d(t) - \frac{1}{n_1} T_f \quad (5.8)$$

$$L \frac{d}{dt} i_a + R i_a = u - K_b n_1 n_2 \dot{y} \quad (5.9)$$

Since the inductance of the motor is extremely small, the current in the motor can be approximated as in Equation (5.10).

$$i_a = \frac{u - K_b n_1 n_2 \dot{y}}{R} \quad (5.10)$$

Plug Equation (5.10) into Equation (5.8) and rearrange the equation, a simplified model is obtained in Equation (5.11).

$$(J_t n_1 n_2 + \gamma m) \ddot{y} + (b n_1 n_2 + \frac{K_t K_b n_1 n_2}{R}) \dot{y} = \frac{K_t}{R} u - \gamma F_{ct} - \gamma d(t) - \frac{1}{n_1} T_f \quad (5.11)$$

Applying Laplace transform on Equation (5.11) results in Equation (5.12).

$$Y(s) = \frac{\frac{K_t/R}{b n_1 n_2 + \frac{K_t K_b n_1 n_2}{R}}}{s \left(\frac{J_t n_1 n_2 + \gamma m}{b n_1 n_2 + \frac{K_t K_b n_1 n_2}{R}} s + 1 \right)} U(s) - \frac{\frac{\gamma}{b n_1 n_2 + \frac{K_t K_b n_1 n_2}{R}}}{s \left(\frac{J_t n_1 n_2 + \gamma m}{b n_1 n_2 + \frac{K_t K_b n_1 n_2}{R}} s + 1 \right)} \left[F_{ct}(s) + d + \frac{1}{\gamma n_1} T_f \right] \quad (5.12)$$

5.2 Rotational Motion

The motor used for rotational motion is the same as the one used for translational motion. Thus, the motor current dynamics will be the same for both subsystems as given in Equation (5.1). The differences between the two subsystems come down to the inertia and the load. Equation (5.13) gives the motor dynamics of the rotation subsystem.

$$J_r \ddot{\theta}_a + b \dot{\theta}_a = T_a - T_L - \frac{1}{n_1} T_D(t) \quad (5.13)$$

$J_r = J_a + J_g + \frac{1}{n_1^2} (2J_c + J_I)$ is the total inertia; J_a is the rotor inertia, J_g is the inertia of the gear box, J_c is the inertia of the gear train on the rack system and J_I is the inertia of the instrument shaft. $T_D(t)$ is the arbitrary bounded disturbance about the motion axis during the operation. The external load T_L in this case comes from the friction, which is provided in Equation (5.14).

$$T_L = \frac{F_{cr} r_E}{n_1} \quad (5.14)$$

F_{cr} is the Coulomb Friction, which can be written as $A_{cr} \cdot \text{sgn}(\dot{\theta}_s)$; r_E is the effective radius of the gear of the gear train to calculate the friction torque.

Plug Equation (5.6) and Equation (5.14) into Equation (5.13), Equation (5.15) is obtained. Plug Equation (5.6) into Equation (5.1), Equation (5.16) is obtained

$$J_r n_1 \ddot{\theta}_s + b n_1 \dot{\theta}_s = K_t i_a - \frac{F_{cr} r_E}{n_1} - \frac{1}{n_1} T_D(t) \quad (5.15)$$

$$L \frac{d}{dt} i_a + R i_a = u - K_b n_1 \dot{\theta}_s \quad (5.16)$$

Current dynamics can be assumed to be instantaneous since the inductance is extremely small, and thus, the current in the motor can be approximated as in Equation (5.17).

$$i_a = \frac{u - K_b n_1 \dot{\theta}_s}{R} \quad (5.17)$$

Plug Equation (5.17) into Equation (5.15) and rearrange the equation, a simplified model is obtained in Equation (5.18).

$$J_r n_1 \ddot{\theta}_s + (b n_1 + \frac{K_t K_b n_1}{R}) \dot{\theta}_s = \frac{K_t}{R} u - \frac{r_E}{n_1} F_{cr} - \frac{1}{n_1} T_D(t) \quad (5.18)$$

Applying Laplace transform on Equation (5.18) results in Equation (5.19).

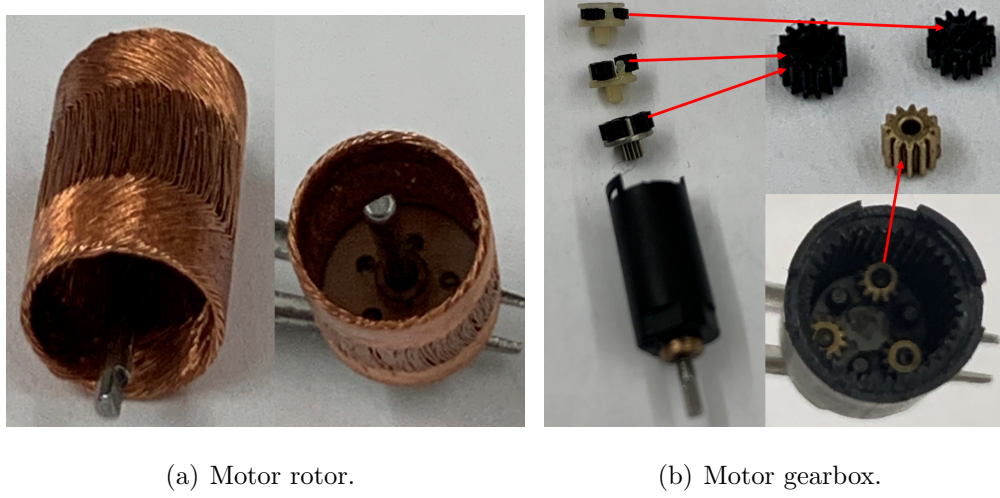
$$\Theta_s(s) = \frac{\frac{K_t/R}{b n_1 + \frac{K_t K_b n_1}{R}}}{s \left(\frac{J_r n_1}{b n_1 + \frac{K_t K_b n_1}{R}} s + 1 \right)} U(s) - \frac{\frac{r_E/n_1}{b n_1 + \frac{K_t K_b n_1}{R}}}{s \left(\frac{J_r n_1}{b n_1 + \frac{K_t K_b n_1}{R}} s + 1 \right)} F_{cr} - \frac{\frac{1/n_1}{b n_1 + \frac{K_t K_b n_1}{R}}}{s \left(\frac{J_r n_1}{b n_1 + \frac{K_t K_b n_1}{R}} s + 1 \right)} T_D(t) \quad (5.19)$$

5.3 System Identification

In this section, system parameters are identified. Some parameters such like the gear ratio and worm gear pitch angle are already known, and the others are determined from measurement and calculation. All the parameters are listed in table 5.1 at the end of this section.

The cylindrical-shell shape motor rotor is shown in (Fig.5.2(a)).

The weight of the rotor is measured to be 0.488 gram. The outer and inner radius is 6.52 mm and 5.62 mm respectively. Applying the inertia equation, J_a can be calculated to be 2.3525e-4 kg · mm².



(a) Motor rotor.

(b) Motor gearbox.

Figure 5.2. Motor components.

There are 4 sets of planetary gear trains in the motor gear box, and they are shown in (Fig.5.2(b)). Using the planetary gear train kinematics and the inertia equation, the total inertia of the gear box is approximated to be $3.96\text{e-}5 \text{ kg}\cdot\text{mm}^2$. This approximation may not be very accurate, but it gives a good start in the parameter estimation.

The weight of the rack system is measured to be 26 grams; the gearbox ratio n_1 is 546:1; n_2 , the gear ratio of the worm gear is $1.25663 \frac{\text{rad}}{\text{mm}}$.

The pitch angle of the worm gear is 38.95° ; the friction coefficient of PLA filament is around 0.4 [28]; L_E is the average value of the outer and inner radius of the worm gear. Thus, γ is calculated using Equation (5.4) to be 0.0021 mm .

The weight and average radius of the worm gear is measured to be 1.358 gram and 2.25 mm respectively. Applying the inertia equation, J_w can be calculated to be $3.4374\text{e-}3 \text{ kg}\cdot\text{mm}^2$.

The resistance of the motor is 7.9Ω . Since the motor or the winding on the rotor is a resistor-inductor circuit, the inductance of the winding can be calculated if the current time constant, $\tau_{ia} = \frac{L}{R}$, is known. In Fig.5.3, the current dynamics is captured

by an oscilloscope. The time constant is $3.3 \mu\text{sec}$, and thus the inductance of the winding is about $26.07 \mu\text{H}$.

To determine the dynamics of the motor, a constant voltage is supplied to the motor. According to Equation (5.1), the steady state voltage u is the sum of resistance voltage Ri_a and the back-EMF voltage $K_b\dot{\theta}_a$. Then the power is cut off, after which the voltage supply u becomes zero, and the current in the motor is induced by the back-EMF voltage. An oscilloscope is bridged on the both sides of the motor to see the voltage change or namely the change of Ri_a , which is shown in Fig.5.4. Note that the term $L\frac{d}{dt}i_a$ is so small that it can be ignored.

Since $K_b\dot{\theta}_a$ is the only voltage source after the power supply is shut off, the voltage dynamics in Fig.5.4 is the dynamics of the motor itself. The time constant is found to be 0.278 second. From Equation (5.2), the time constant of the motor is equal to $\frac{J}{b}$; namely, the ratio between the motor inertia and the viscous damping coefficient is known as to be 0.278 second.



Figure 5.3. The rise in the current.

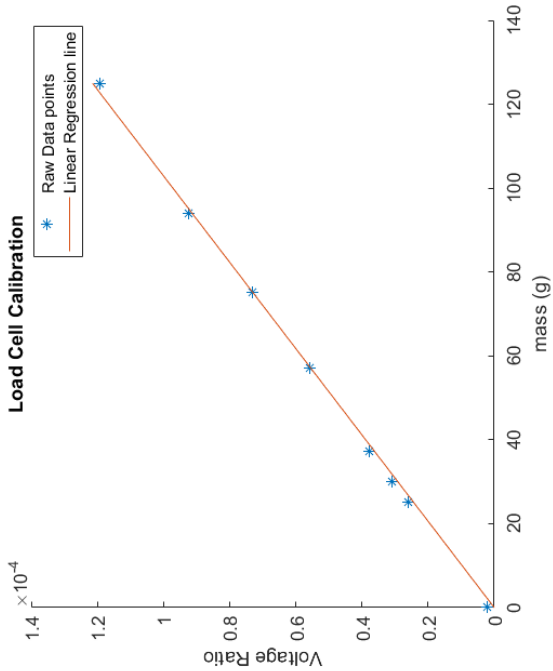
The motor constant K_t is determined using a load cell, of which the calibration plot is given in (Fig.5.5(b)). The calibration setup is given in (Fig.5.5(a)).

As shown in Fig 5.5(a), different weights are used to calibrate the load cell. The weight is placed on a white holder, which is hanged still using fishing wire. The fishing wire is connected to the load cell and pass upon a pulley and a groove 3D-printed by the author. The groove is used to test the motor torque, and therefore the fish line should be passing upon it to make sure the calibration is correct for the future testing.

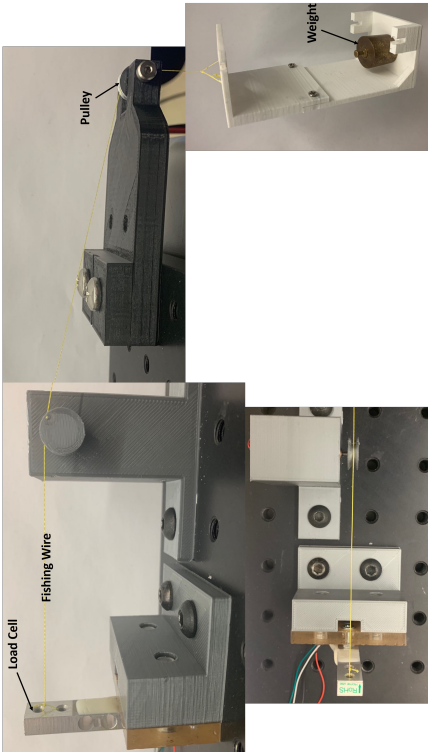
In (Fig.5.5(b)), the voltage ratio of the load cell terminals is plotted against the weight of the mass. The * represents the raw data points of each measurement ranging from 1 gram to 125 grams, and the line is obtained from least square fitting method. The equation of the linear regression line is: $y = 2.35 \times 10^{-6} + 0.7158 \times 10^{-7}x$, in which y is the voltage ratio and x is the weight of the mass.



Figure 5.4. Motor Voltage drop after power supply is shut down.

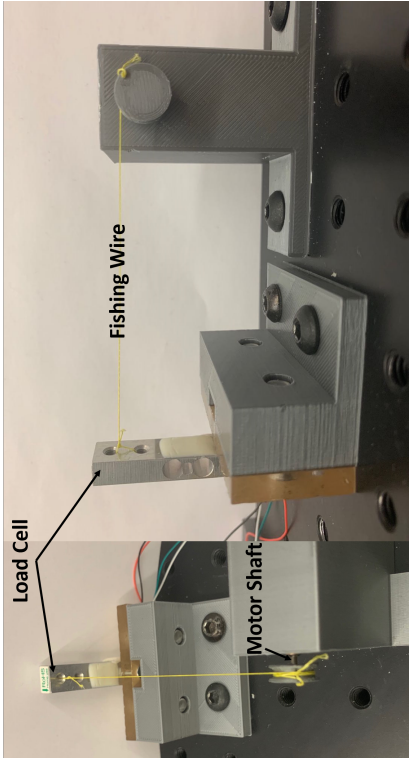


(b) Regression on the load cell voltage.

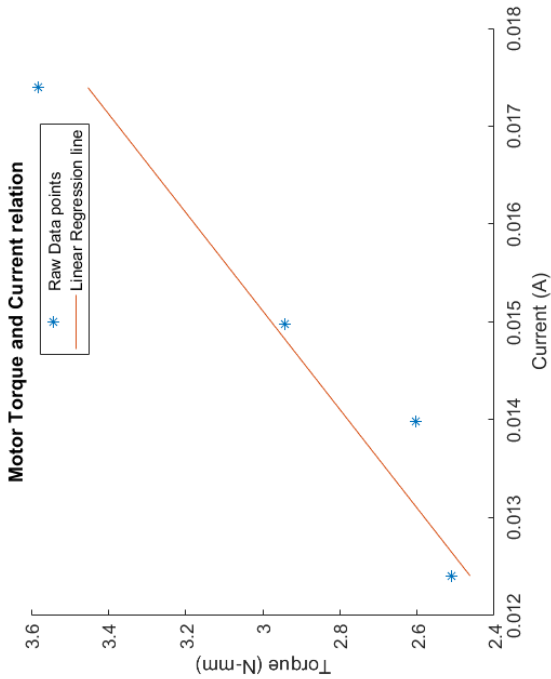


(a) Calibration Setup.

Figure 5.5. Calibration on the load cell.



(a) Motor constant measurement setup.



(b) Regression of the motor constant.

Figure 5.6. Measurement of the motor constant.

After calibration, similar setup shown in (Fig.5.6(a)) is used to get the motor constant K_t . One end of the fishing wire is tied tightly on the groove, and the other end is on the load cell. The motor is supplied with constant current using the lab DC power supply and thus the motor will output constant torque. The load cell will then output a constant voltage ratio, which can be converted to the torque being applied. (Fig.5.6(b)) plots the torque against current, and the slope is the motor constant K_t , which is $198.5 \frac{N \cdot mm}{amp}$.

The back-EMF ratio K_b is not a constant; rather, it is an exponential decay function of the armature current as shown in Fig.5.7. The equation is $K_b = 0.0003e^{-5.401i_a}$.

Friction of this system in either the translation system or rotation system is hard to model with an analytical equation, and thus it is rather bounded by the lower and upper limits from the experiment.

In summary of this section, all the parameters being estimated are listed in Table 5.1. These values may not be very accurate but will be a good start.

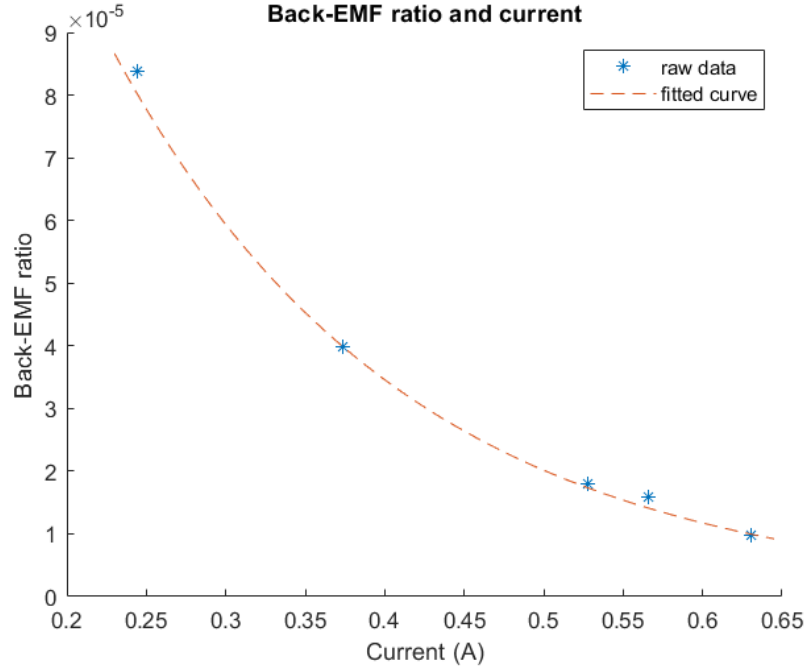


Figure 5.7. Relationship between the armature current and the Back-EMF ratio.

Table 5.1. System Parameters.

Parameter	Symbol	Value (range)	Unit
Gearbox ratio	n_1	546	None
Worm gear ratio	n_2	1.25663	$\frac{rad}{mm}$
Rack system Mass	m	0.026	kg
Worm gear Mass	m_w	1.358e-3	kg
Motor Gear Mass	m_{c1}	4.3e-4	kg
Shaft Gear Mass	m_{c2}	1.09 e-3	kg
Shaft Mass	m_I	6.332e-3	kg
Rotor inertia	J_a	2.3525e-4	$kg \cdot mm^2$
Gear box inertia	J_g	3.96e-5	$kg \cdot mm^2$
Worm gear inertia	J_w	3.4374e-3	$kg \cdot mm^2$
Motor gear inertia	J_{c1}	0.0215	$kg \cdot mm^2$
Shaft gear inertia	J_{c2}	0.0142	$kg \cdot mm^2$
Total inertia of translation system	J_t	0.0045	$kg \cdot mm^2$
Total inertia of rotation system	J_r	0.0045	$kg \cdot mm^2$
Motor viscous damping ratio	b	0.0066	$N \cdot mm \cdot sec$
Motor resistance	R	7.9	Ω
Motor inductance	L	26.04	μH
Torque to force ratio	γ	0.0021	mm
Motor constant	K_t	198.5	$\frac{N \cdot mm}{A}$
Back-EMF ratio	K_b	$f(i_a)$	$\frac{V}{rad/sec}$
Gear radius of rotation system	R_e	6.34	mm

5.4 Model Validation

In this section, the models derived before are validated using experimental position and speed data at normal operation point of the device. Closed loop responses under proportional controller are achieved using different input signal.

(Fig.5.8) shows the closed loop speed response of both simulated system and real system when the reference is a sinusoidal signal and a proportional controller is applied.

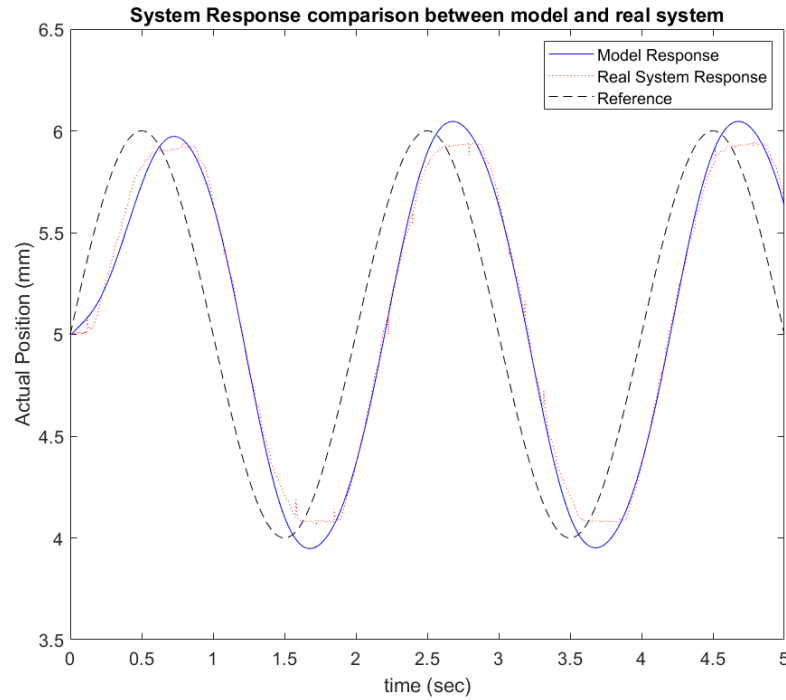


Figure 5.8. Translational position Response under sinusoidal reference.

The position response of the model is quite accurate except for not depicting the flat region at each peak of the real response. This further indicates that the friction has a high non-linearity. The modeled Coulomb friction cannot completely describe the true friction, which is of a high non-linearity. After all, the model is in a good shape with a small parameter uncertainties and structure uncertainty in friction.

Like the translation system, the same validation procedure is applied to the rotation system. (Fig.5.9) shows the closed loop speed response of both simulated system and real system when the reference is a sinusoidal signal and a proportional controller is applied.

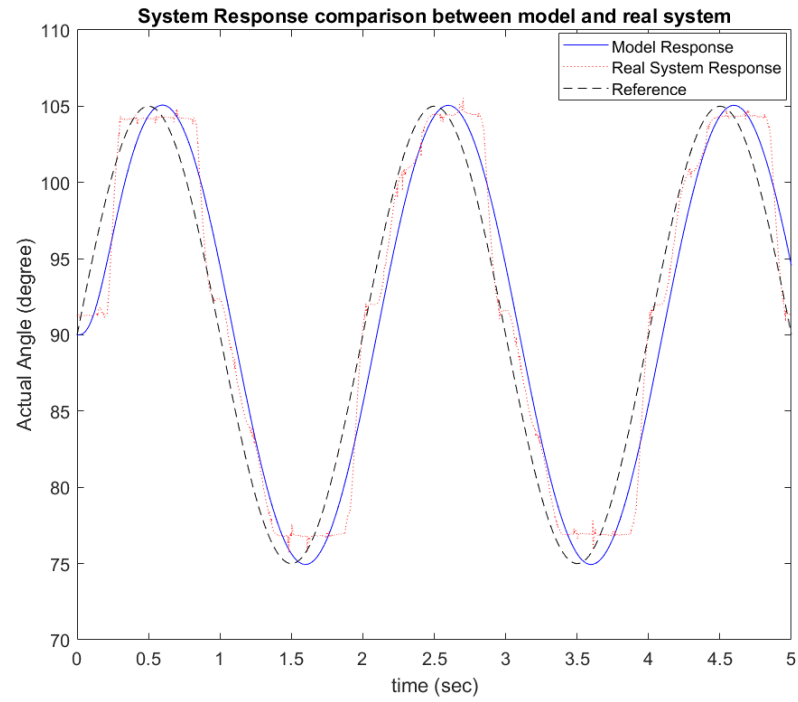


Figure 5.9. Rotational position Response under sinusoidal reference.

Again there is flat region at each peak of the real system response, and this implies that the nonlinear friction also exists in the rotation system.

6. CONTROL ALGORITHM DESIGN

In this chapter, the requirements for the motion control are introduced and the models are derived. Control algorithms used to track position and speed are developed for both the rotational and translational systems. Kalman filter is also developed to better estimate the states of the system. Simulation and real system responses are given in the next two chapters respectively.

6.1 Requirements

The position of the translational and rotational motion need to be controlled. For precise position control, it is desired to choose feedback sensors with a resolution less than or equal to $10\text{ }\mu\text{m}$. There should be minimal overshoot, and the steady-state error of $50\text{ }\mu\text{m}$ or less is desired for a reference step input. Similarly, the feedback sensor resolution requirement for rotational motion should be less than or equal to 0.1° . A minimal overshoot and the steady-state error less than or equal to 2° is desired in step reference tracking. Furthermore, the 2% settling time for both system should be less or equal to 2 second; or namely the real response should be able to track a reference signal with a cut-off frequency of a 2 rad/sec.

6.2 Position Tracking Controller Design

In this section, position tracking algorithm is developed for the rotational as well as translational motion of the instrument shaft.

6.2.1 Translation

Deterministic Robust Controller can handle the situation when both the parameter uncertainty and the structure uncertainty such like the known bounded mismatch in the parameters, bounded arbitrary disturbance, bounded nonlinear friction exist, and this type of controller guarantees a very small, if not zero, error [29, 30].

Equation (6.1) is obtained from Equation (5.11) through changing variables.

$$M\ddot{y} = Ku - B\dot{y} - \frac{1}{n_1}T_f - \gamma F_{ct} - \gamma d(t) \quad (6.1)$$

where $M = J_t n_1 n_2 + \gamma m$, $B = b n_1 n_2 + \frac{K_t K_b n_1 n_2}{R}$, $K = \frac{K_t}{R}$.

Let error $e = y - y_d$ be the difference between the actual position and reference position, and the augmented error is $p = \dot{e} + k_1 e$, which can be combined with Equation (6.1) to obtain Equation (6.2).

$$M\dot{p} = Ku - B\dot{y} - \frac{1}{n_1}T_f - \gamma F_{ct} - \gamma d(t) - M(\ddot{y}_d - k_1 \dot{e}) = Ku + \varphi^T \theta \quad (6.2)$$

$$\varphi = \begin{bmatrix} -\dot{y} & -\frac{1}{n_1} & -\text{sgn}(\dot{y}) & -1 & -(\ddot{y}_d - k_1 \dot{e}) \end{bmatrix}^T \quad (6.3)$$

$$\theta = [B \quad T_f \quad \gamma A_{sc} \quad \gamma d(t) \quad M]^T \quad (6.4)$$

The control effort u has three components: $u = u_a + u_s + u_p$. u_a is the model reference compensation given in Equation (6.22). u_s is the model uncertainty compensation given in Equation (6.32). u_p is used to keep the stability given in Equation (6.34).

$$u_a = -\frac{1}{\hat{K}} \varphi^T \hat{\theta} \quad (6.5)$$

$$\hat{\theta} = [\hat{B} \quad T_{f0} \quad \hat{\gamma} \hat{A}_{sc} \quad \hat{\gamma} d_0 \quad \hat{M}]^T \quad (6.6)$$

d_0 is a nominal disturbance value.

$$u_s = -(h(x, t) + h_0) \operatorname{sgn}(p) \quad (6.7)$$

$$h(x, t) = |\varphi^T| \left(\frac{\hat{\theta}_{max}}{\hat{K}_{min}} - \frac{\hat{\theta}_{min}}{\hat{K}_{max}} \right) \quad (6.8)$$

h_0 is a proper positive number.

$$u_p = -\frac{k_2}{\hat{K}} p \quad (6.9)$$

6.2.2 Rotation

From Equation (5.18), Equation (6.10) can be obtained.

$$J\ddot{\theta}_s + B\dot{\theta}_s = Ku - \frac{r_E}{n_1} F_{cr} - \frac{1}{n_1} T_D(t) \quad (6.10)$$

where $J = J_r n_1$, $B = b n_1 + \frac{K_t K_b n_1}{R}$, $K = \frac{K_t}{R}$.

Let error $e = \theta_s - \theta_{sd}$ be the difference between the actual angle and reference angle, and the augmented error is $p = \dot{e} + k_1 e$, which can be combined with Equation (6.10) to obtain Equation (6.11).

$$J\dot{p} = Ku - B\dot{\theta}_s - \frac{r_E}{n_1} F_{cr} - \frac{1}{n_1} T_D(t) - J(\ddot{\theta}_{sd} - k_1 \dot{e}) = \varphi^T \theta \quad (6.11)$$

$$\varphi = \left[-\dot{\theta}_s \quad -\frac{R_E}{n_1} \operatorname{sgn}(\dot{\theta}_s) \quad -\frac{1}{n} \quad -(\ddot{\theta}_{sd} - k_1 \dot{e}) \right]^T \quad (6.12)$$

$$\theta = [B \quad A_{sc} \quad T_D(t) \quad J]^T \quad (6.13)$$

The control effort u has three components: $u = u_a + u_s + u_p$. u_a is the model reference compensation given in Equation (6.30). u_s is the model uncertainty compensation given in Equation (6.32). u_p is used to keep the stability given in Equation (6.34).

$$u_a = -\frac{1}{\hat{K}}\varphi^T\hat{\theta} \quad (6.14)$$

$$\hat{\theta} = \begin{bmatrix} \hat{B} & \hat{A}_{sc} & T_{D0} & \hat{J} \end{bmatrix}^T \quad (6.15)$$

T_{D0} is a nominal torque disturbance value.

$$u_s = -(h(x, t) + h_0) \operatorname{sgn}(p) \quad (6.16)$$

$$h(x, t) = |\varphi^T| \left(\frac{\hat{\theta}_{max}}{\hat{K}_{min}} - \frac{\hat{\theta}_{min}}{\hat{K}_{max}} \right) \quad (6.17)$$

h_0 is a proper positive number.

$$u_p = -\frac{k_2}{\hat{K}}p \quad (6.18)$$

6.3 Speed Tracking Controller Design

In this section, speed tracking algorithm is developed for the rotational as well as translational motion of the instrument shaft. The only difference between the speed tracking and the position tracking is the augmented error dynamics, which in the first order speed model is the actual error between the actual speed and desired one.

6.3.1 Translation

For the translational speed tracking, the error is changed to be $e = v - v_d$, where $v = \dot{y}$ and v_d is the desired speed, and thus $p = e = v - v_d$, which can be combined with Equation (6.2) to arrive at Equation (6.19).

$$M\dot{p} = Ku - B\dot{y} - \frac{1}{n_1}T_f - \gamma F_{ct} - \gamma d(t) - M\dot{v}_d = \varphi^T\theta \quad (6.19)$$

$$\varphi = \begin{bmatrix} -\dot{y} & -\frac{1}{n_1} & -\operatorname{sgn}(\dot{y}) & -1 & -\dot{v}_d \end{bmatrix}^T \quad (6.20)$$

$$\theta = [B \quad T_f \quad \gamma A_{sc} \quad \gamma d(t) \quad M]^T \quad (6.21)$$

Following similar steps as in the position tracking DRC algorithm, three control efforts u_a , u_s and u_p can be achieved.

$$u_a = -\frac{1}{\hat{K}} \varphi^T \hat{\theta} \quad (6.22)$$

$$\hat{\theta} = [\hat{B} \quad T_{f0} \quad \hat{\gamma} \hat{A}_{sc} \quad \hat{\gamma} d_0 \quad \hat{M}]^T \quad (6.23)$$

d_0 is a nominal disturbance value.

$$u_s = -(h(x, t) + h_0) \operatorname{sgn}(p) \quad (6.24)$$

$$h(x, t) = |\varphi^T| \left(\frac{\hat{\theta}_{max}}{\hat{K}_{min}} - \frac{\hat{\theta}_{min}}{\hat{K}_{max}} \right) \quad (6.25)$$

h_0 is a proper positive number.

$$u_p = -\frac{k_2}{\hat{K}} p \quad (6.26)$$

6.3.2 Rotation

For the rotational speed tracking, the error is changed to be $e = \omega - \omega_d$, where $\omega = \dot{\theta}_s$ and ω_d is the desired speed, and thus $p = e = \omega - \omega_d$, which can be combined with Equation (6.10) to arrive at Equation (6.27).

$$J\dot{p} = Ku - B\dot{\theta}_s - \frac{r_E}{n_1} F_{cr} - \frac{1}{n_1} T_D(t) - J\dot{\omega}_d = \varphi^T \theta \quad (6.27)$$

$$\varphi = \begin{bmatrix} -\dot{\theta}_s & -\frac{R_E}{n_1} \operatorname{sgn}(\dot{\theta}_s) & -\frac{1}{n} & -(\dot{\omega}_d) \end{bmatrix}^T \quad (6.28)$$

$$\theta = [B \quad A_{sc} \quad T_D(t) \quad J]^T \quad (6.29)$$

Following similar steps as in the angular position tracking DRC algorithm, three control efforts u_a , u_s and u_p can be achieved.

$$u_a = -\frac{1}{\hat{K}}\varphi^T\hat{\theta} \quad (6.30)$$

$$\hat{\theta} = [\hat{B} \quad \hat{A}_{sc} \quad T_{D0} \quad \hat{J}]^T \quad (6.31)$$

T_{D0} is a nominal torque disturbance value.

$$u_s = -(h(x, t) + h_0) \operatorname{sgn}(p) \quad (6.32)$$

$$h(x, t) = |\varphi^T| \left(\frac{\hat{\theta}_{max}}{\hat{K}_{min}} - \frac{\hat{\theta}_{min}}{\hat{K}_{max}} \right) \quad (6.33)$$

h_0 is a proper positive number.

$$u_p = -\frac{k_2}{\hat{K}}p \quad (6.34)$$

6.4 Kalman Filter

In this section, Kalman filter is developed for both translation and rotation system given the nominal system parameters listed in Table 5.1.

Ignoring the nonlinear part, the translation model can be written in a state space representation with:

$$A = \begin{pmatrix} 0 & 1 & 0 \\ 0 & \frac{-B}{M} & \frac{K}{M} \\ 0 & -K_b n_1 n_2 & \frac{-R}{L} \end{pmatrix} \quad (6.35)$$

$$B = \begin{pmatrix} 0 & 0 & \frac{1}{L} \end{pmatrix}^T \quad (6.36)$$

$$C = \begin{pmatrix} 1 & 0 & 0 \end{pmatrix} \quad (6.37)$$

where: $M = J_t n_1 n_2 + \gamma m$, $B = b_1 n_1 n_2$, $K = K_t$.

The state variables are $x = (y \ \dot{y} \ i_a)^T$, corresponding to the position, speed and current.

After plugging in the parameter value, the above continuous state space model is converted into a discrete model with a sampling rate of 2kHz. Then using the following set of the recursive equations, Kalman states $\hat{x}(k | k)$ can be achieved.

$$\hat{x}(k | k - 1) = A_d \hat{x}(k - 1 | k - 1) + B_d u(k - 1) \quad (6.38)$$

$$M = A_d \cdot Z(k - 1) \cdot A_d^T + Q \quad (6.39)$$

Q in the above equation is the process covariance matrix. The larger this matrix is, the more correction is given by the Kalman Filter on the model prediction based on the measurement; namely, if the model uncertainty or the external disturbance is large, then the Q matrix should be large as well to compensate the model error using the feedback.

$$L_{KF}(k) = M \cdot C_d^T \cdot (C_d \cdot M \cdot C_d^T + V)^{-1} \quad (6.40)$$

V is the white noise variance, and this value is to be measured through experiment.

$$\hat{x}(k | k) = \hat{x}(k | k - 1) + L_{KF}(k) \cdot (y(k) - C_d \hat{x}(k | k - 1)) \quad (6.41)$$

$$Z(k) = (I - L_{KF}(k) \cdot C_d) \cdot M \quad (6.42)$$

Following similar approach, the Kalman Filter for the rotation system can be developed.

7. SIMULATION

In this chapter, the system models, which include the current dynamics, from the model section are simulated in MATLAB. Different control algorithms including the DRC, PID controller and Loop-Shaping Controller are implemented to drive the system model, and the performance among those control algorithms are compared. Author provides two different scenarios: when there are no real life problems such as noise and when there are real life problems. In the ideal case, the state feedback is the true state and the external disturbance, noise, quantization error, signal delay due to filter are not considered; oppositely, in the real case, Position is the only state being fed back and external disturbance, noise, quantization error, signal delay are considered. Reader can get to know how each of those real life problems can affect the system response: in general, quantization error causes larger steady-state error; signal delay from the filter induces overshoot; noise increases the steady-state oscillation; frequent disturbance does not have large impact in the translation system, but the rotation system is affected in a greater amount. At the end of the chapter, the proper controllers for position and speed tracking are to be selected for the real implementation.

7.1 Translation System

This section covers the comparison among the performance of different controllers in translational position tracking and speed tracking. The performance among DRC, PID controller and Inverse-based Loop-Shaping controller are compared given a model reference input. Both ideal case and real case are demonstrated in this section, and discussions are also included.

(Fig.7.1) shows the position tracking performance of all three controllers in the ideal case. In the ideal case, DRC can follow up the reference quite well and constrains the transient and steady-state error to be very small; in contrast, PID controller and the Loop-Shaping controller lose the track on the reference in the transient state and only converges to the steady-state reference value.

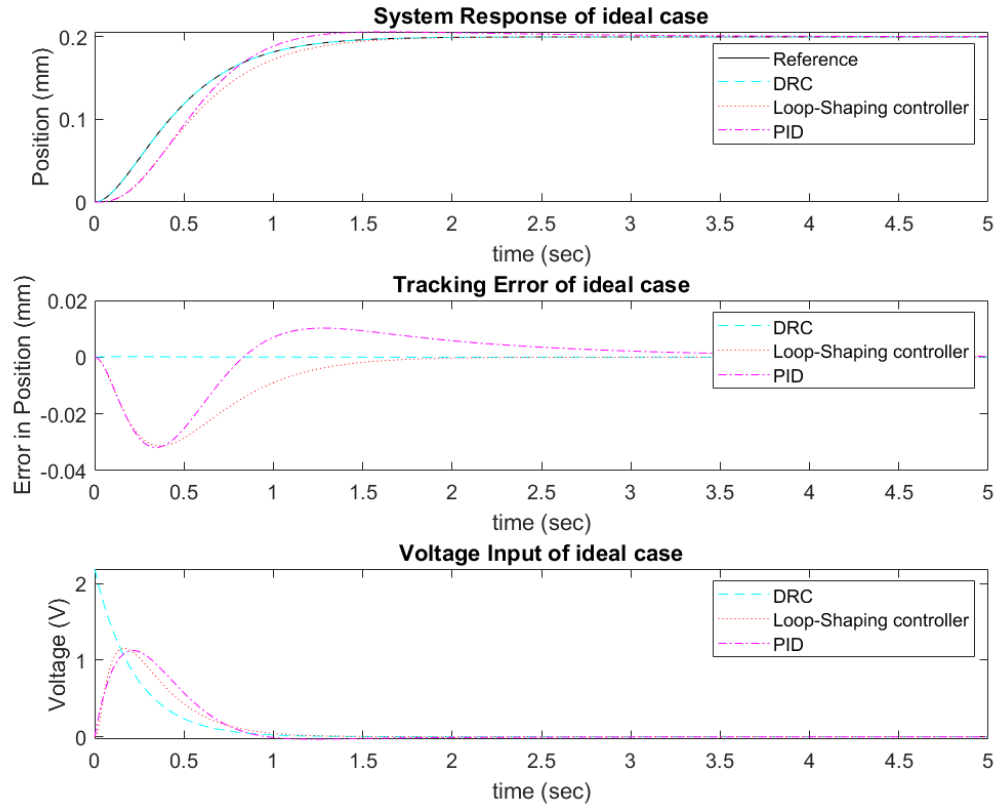


Figure 7.1. Translational position tracking performance in ideal situation.

(Fig.7.2) shows the position tracking performance of all three controllers in the real case. In the real case, the presence of the quantization in both the voltage input and sensor feedback, induces a constant steady state error for all control algorithms and the magnitude is about the same as the quantization error. The control effort of PID controller is affected most severely by the quantization error. With the help

of the Kalman Filter, which does have some model uncertainty, the noise effect is significantly reduced. DRC performs the best among the three controllers with a small overshoot, caused by the signal delay due to the model uncertainty in Kalman Filter, at very beginning.

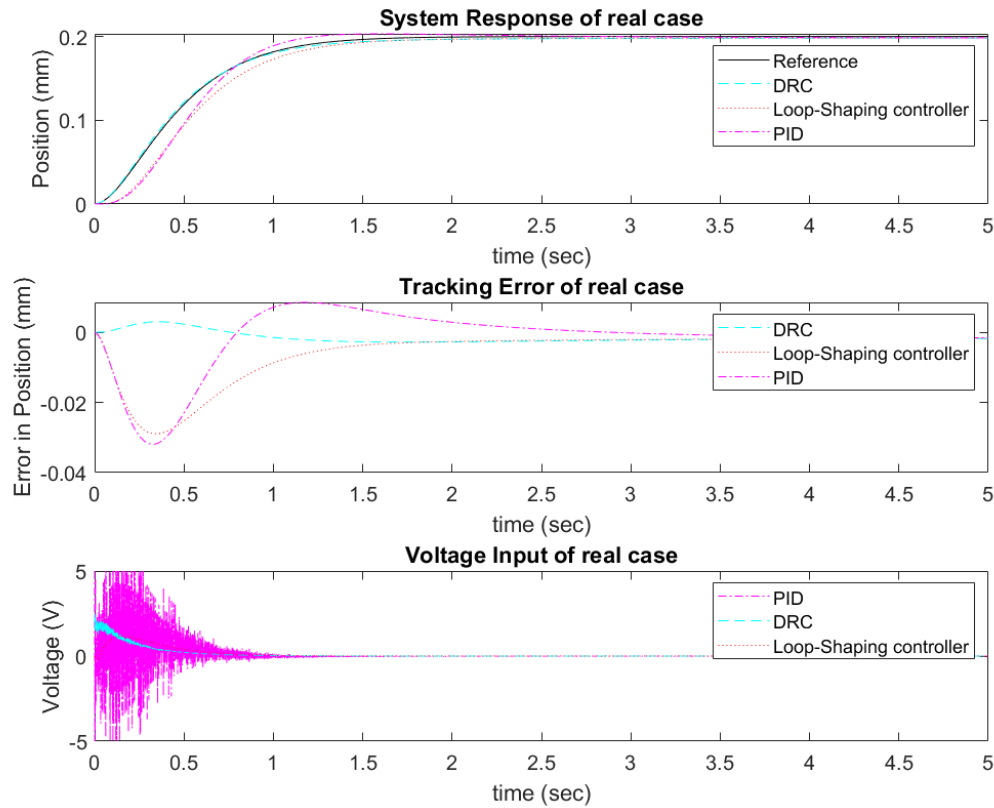


Figure 7.2. Translational position tracking performance in real situation.

(Fig.7.3) shows the speed tracking performance of all three controllers in the ideal case. In the ideal case, PID controller has a smaller error in both steady and transient state compared to other two control algorithms. In addition, the voltage input is also smoother for the PID controller. Unlike position tracking, in which DRC does a better job, speed tracking is accomplished by PID controller. The reason behind is

that DRC is more suitable for a higher order system such like the position plant while PID controller is better if the system order is lower.

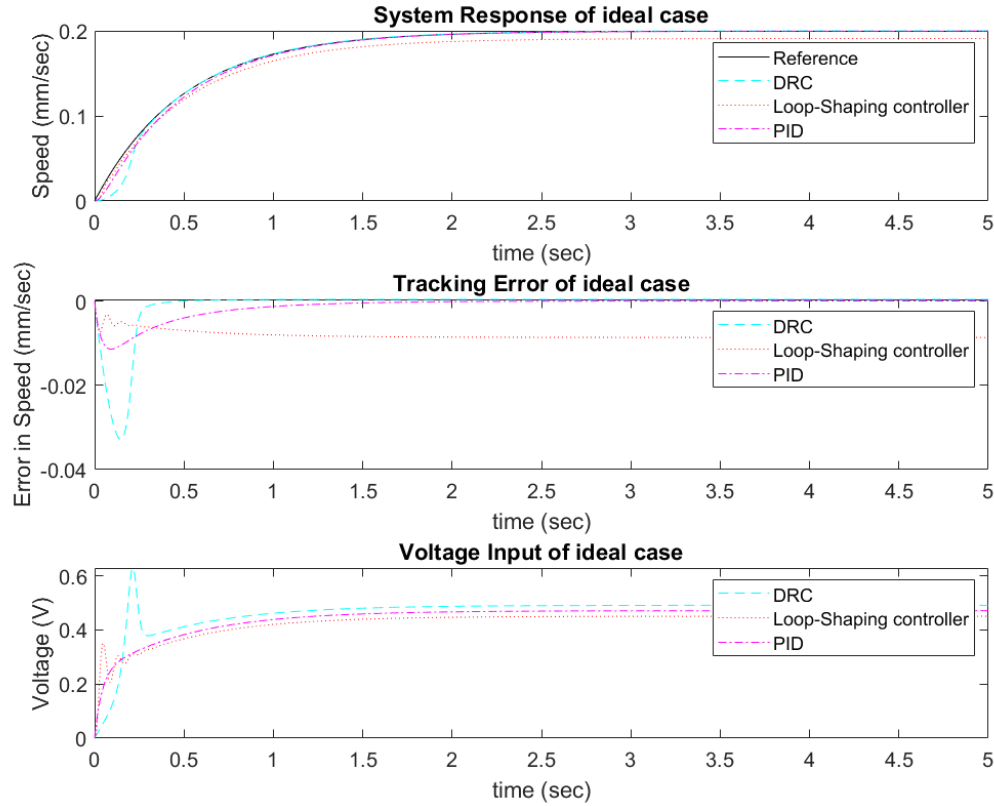


Figure 7.3. Translational speed tracking performance in ideal situation.

(Fig.7.4) shows the speed tracking performance of all three controllers in the real case. In the real case, a Kalman Filter with model uncertainty is used to predict the unknown speed state. It can be seen that the controlled speed does not converge to the true speed of the system and this is because of the model uncertainty. When the model uncertainty exists, Kalman filter will not predict very well unless the process variance matrix is set to be of large magnitude and the feedback is accurate enough to correct the model state prediction. In this case, the process covariance matrix is not added, and therefore the predicted value is not corrected. Thus, if the model uncertainty is

not minimized, Kalman Filter will not predict well in the state especially the speed; namely, the controlled response will rather converge to a wrong state value and thus error is induced.

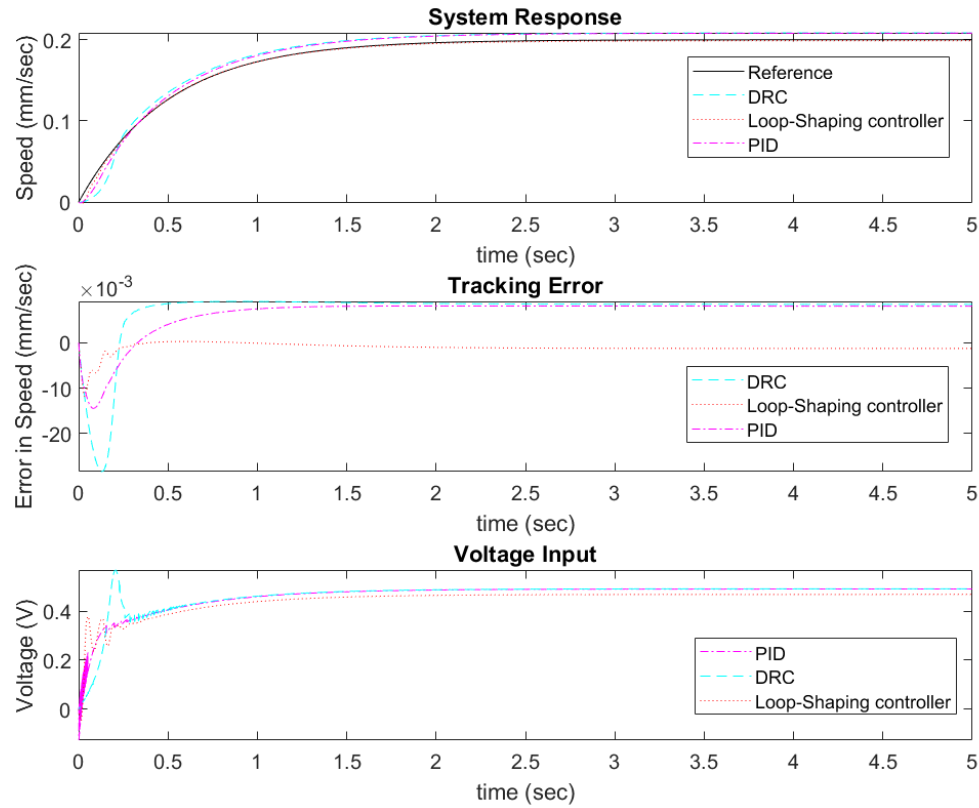


Figure 7.4. Translational speed tracking performance in ideal situation.

After comparing the simulation result, DRC works better in the position tracking while PID controller works better in the speed tracking.

7.2 Rotation System

This section covers the comparison among the performance of different controllers in rotational position tracking and speed tracking. The performance among DRC, PID controller and Inverse-based Loop-Shaping controller are compared given a model

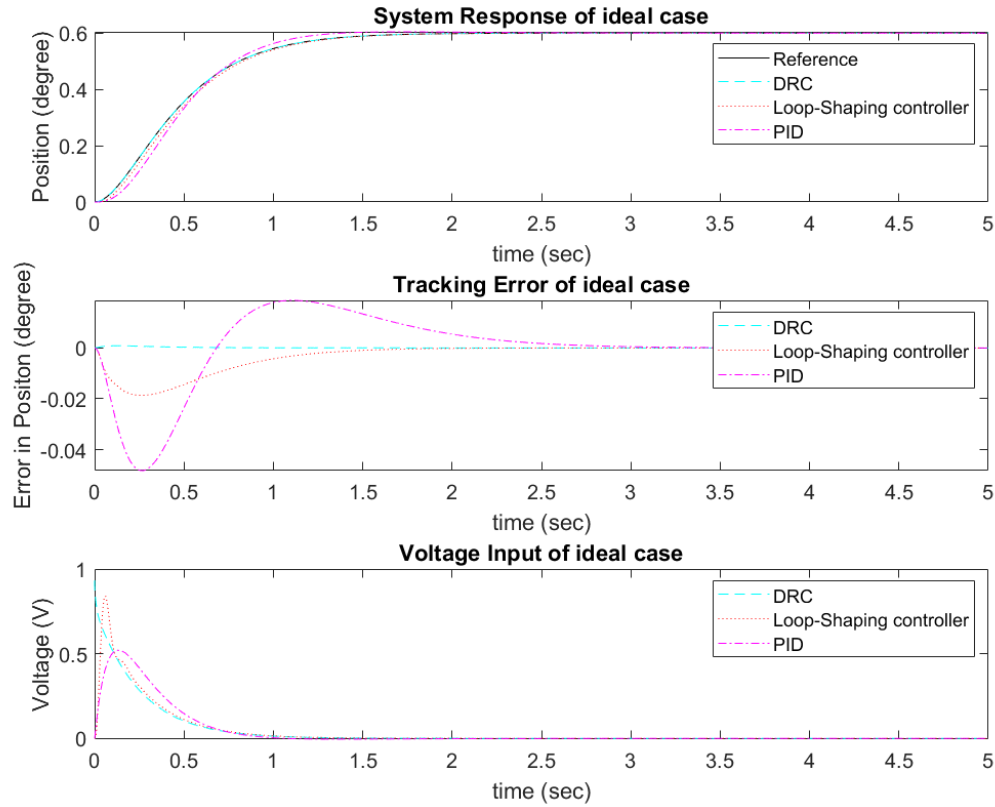


Figure 7.5. Angular position tracking performance in ideal situation.

reference input. Both ideal case and real case are demonstrated in this section, and discussions are also included.

(Fig.7.5) shows the position tracking performance for rotation system in ideal case. In the ideal case, DRC can follow up the reference quite well and constrains the transient and steady-state error to be very small; in contrast, PID controller and the Loop-Shaping controller lose the track on the reference in the transient state and only converges to the steady-state reference value.

(Fig.7.6) shows the position tracking performance for rotation system in real case. In the real case, the presence of the quantization in both the voltage input and sensor feedback, induces a constant steady state error for all control algorithms and

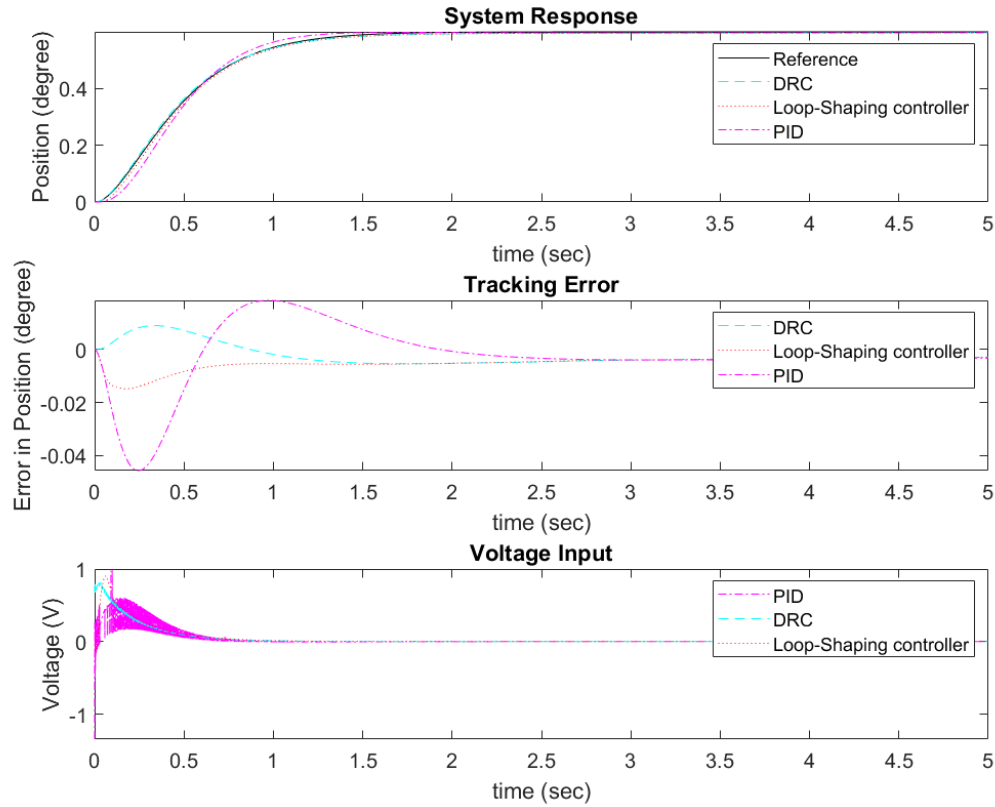


Figure 7.6. Angular position tracking performance in real situation.

the magnitude is about the same as the quantization error. The control effort of PID controller is affected most severely by the quantization error. With the help of the Kalman Filter, which does have some model uncertainty, the noise effect is significantly reduced. DRC performs the best among the three controllers with a small overshoot, caused by the signal delay due to the model uncertainty in Kalman Filter, at very beginning.

(Fig.7.7) shows the speed tracking performance of all three controllers in the ideal case. In the ideal case, PID controller has a smaller error in both steady and transient state compared to other two control algorithms. In addition, the voltage input is also smoother for the PID controller. Unlike position tracking, in which DRC does a

better job, speed tracking is accomplished by PID controller. The reason behind is that DRC is more suitable for a higher order system such like the position plant while PID controller is better if the system order is lower.

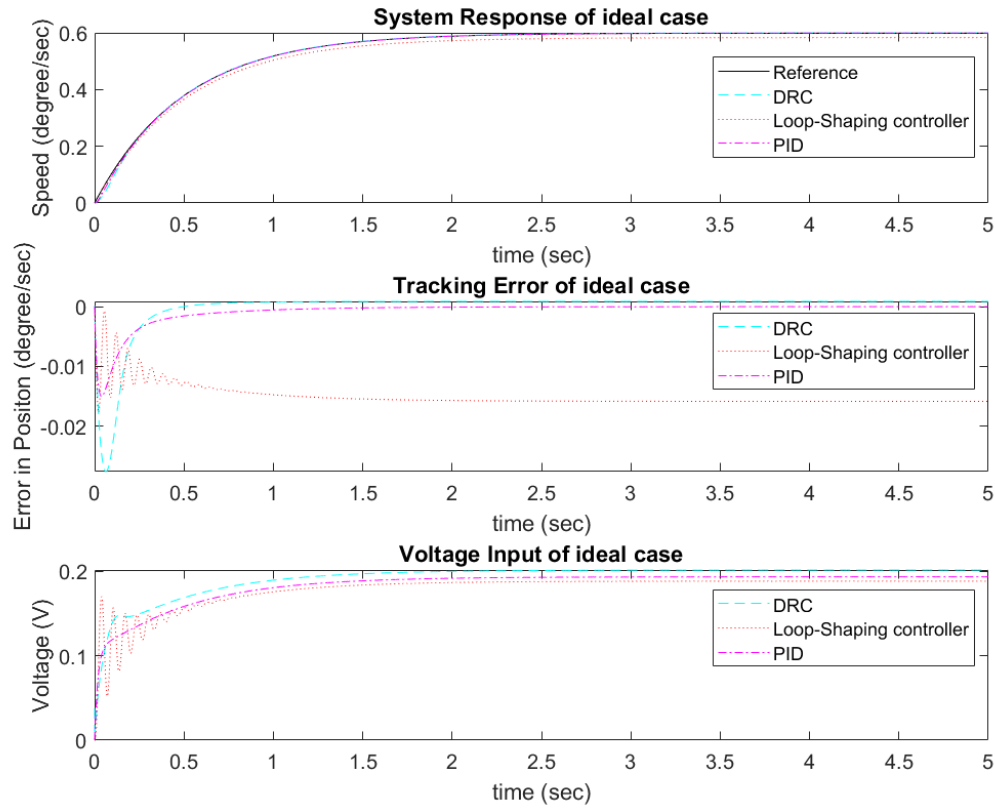


Figure 7.7. Angular speed tracking performance in ideal situation.

(Fig.7.8) shows the speed tracking performance of all three controllers in the real case. Similarly, Kalman Filter with model uncertainty fails to correctly describe the true state, and a process covariance matrix is needed to correct the model prediction using the incoming feedback, which needs to be accurate. Still, DRC is good for position tracking and PID works well in speed tracking.

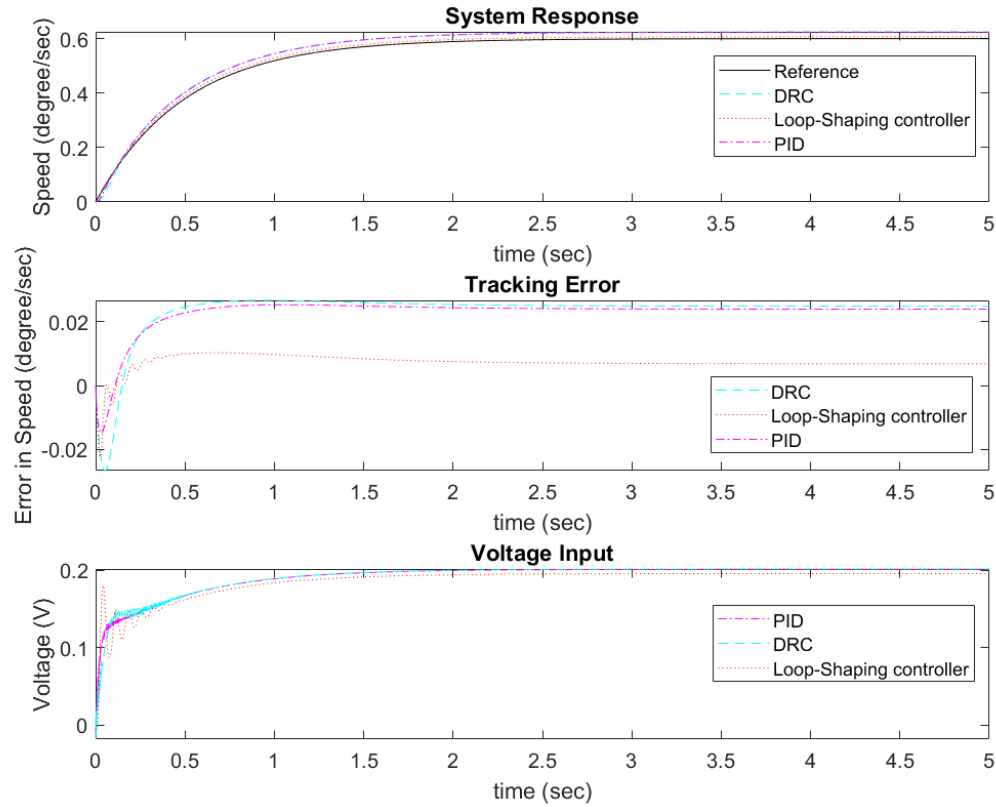


Figure 7.8. Angular speed tracking performance in ideal situation.

To summarize this chapter, DRC is suitable for the position tracking while PID controller works better in speed tracking. Kalman filter is necessary to better estimate the system states and to get rid of the discontinuity induced by quantization error.

8. EXPERIMENTAL RESULTS

In this chapter, the system responses from the prototype are presented. From the previous chapter, author concluded that, among the three simulated controller, DRC controller coupled with Kalman Filter is the best combination that yields good position tracking performance in the real situation and PID controller is the best in speed tracking in the real situation. Thus in the real implementation, with the Kalman filter, DRC is applied to do position tracking and PID is used to do the speed tracking.

The potentiometers used for measurement were calibrated using an overhead camera system with a known image pixel to micron conversion ratio. The range for the linear potentiometer is 12.7 mm while the range for the rotary potentiometer is 180°. Once the sensors are calibrated and the control parameters estimated, the controllers were implemented to the system and the controlled performance of the system is analyzed.

8.1 Translation System

In this section, the position and speed tracking responses are provided and the performance is discussed. (Fig.8.1) shows the position tracking response in the translational motion as well as the tracking error.

The plot at the left of (Fig.8.1) shows actual position and reference position versus time. The actual response is quite smooth without obvious oscillation in spite of some random noise. On the right side of (Fig.8.1) shows the position tracking error along time. It can be observed that the transient error is larger than the steady state error but still constrained with 200 microns. The steady state error is bounded within 10 microns and it cannot be reduced further due to the effect of quantization error, which is discussed in the previous chapter. There must be uncertainties in the model

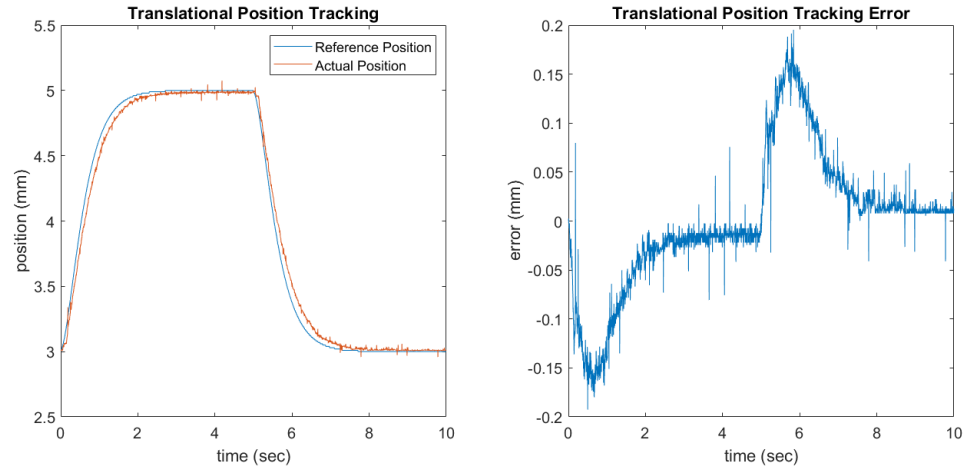


Figure 8.1. Position tracking performance in translational motion.

since the system lose track on the reference during the transient state. There is no overshoot during the tracking, and this implies that the Kalman position, if not all the states, stays quite close to the true position of the translation system.

(Fig.8.2) shows the speed tracking response in the translational motion as well as the tracking error.

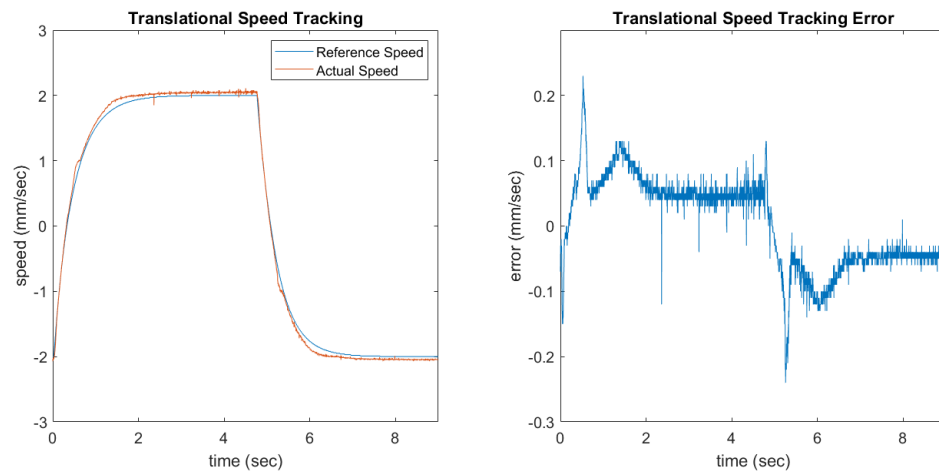


Figure 8.2. Speed tracking performance in translational motion.

The plot at the left of (Fig.8.2) shows actual speed and reference speed versus time. The actual response is quite smooth without obvious oscillation in spite of some random noise. There is overshoot between the transient state and the steady state, and this implies that the Kalman speed signal is lagged from the true speed. On the right side of (Fig.8.2) shows the speed tracking error along time. It can be observed that the transient error is larger than the steady state error but still constrained with 300 microns/sec. The steady state error is bounded within 100 microns/sec and it cannot be reduced further due to the effect of quantization error, which is discussed in the previous chapter.

8.2 Rotation System

In this section, the position and speed tracking responses for the rotation system are provided, and the performance is discussed. (Fig.8.3) shows the position tracking response in the rotational motion as well as the tracking error.

The plot at the left of (Fig.8.3) shows actual position and reference position versus time. There are some slight oscillations during the transient state, but these are within tolerance. Overall, the actual response is quite smooth in spite of some random

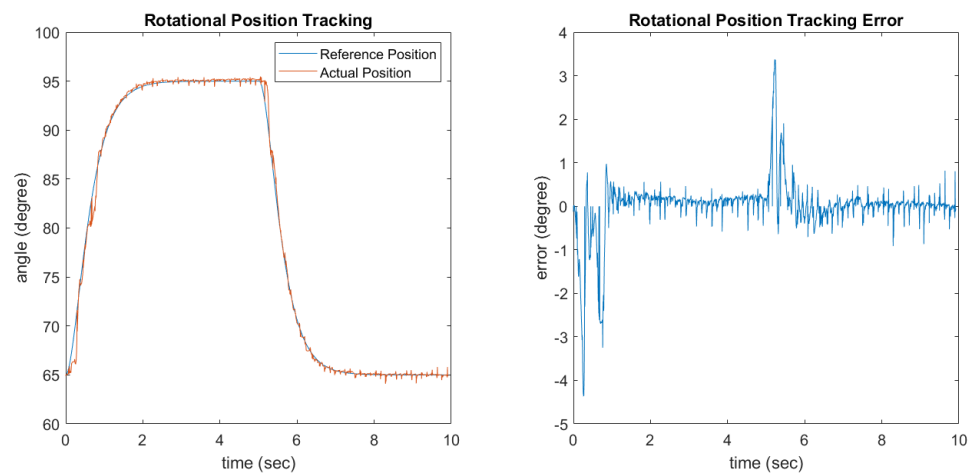


Figure 8.3. Position tracking performance in rotational motion.

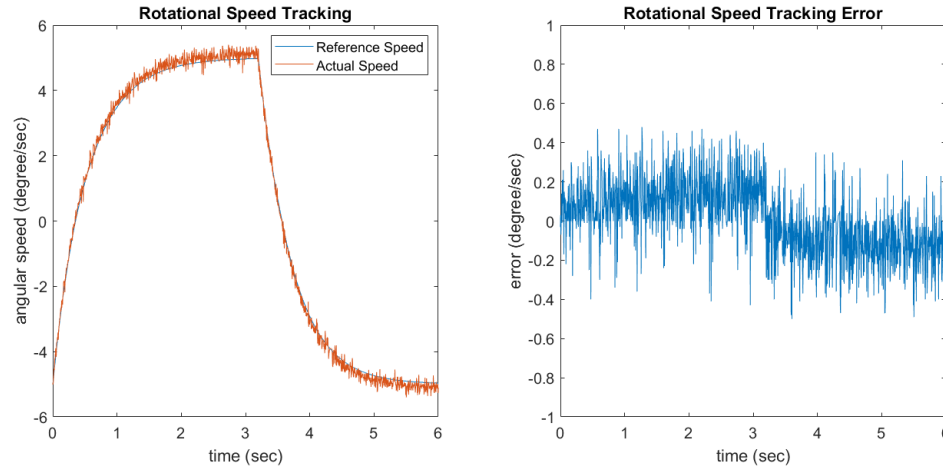


Figure 8.4. Speed tracking performance in rotational motion.

noise. On the right side of (Fig.8.3) shows the angle tracking error along time. It can be observed that the transient error is larger than the steady state error but still constrained within 4 degrees. The steady state error is bounded within 0.5 degree. This large error is caused by model uncertainty and the badly manufactured gear trains.

(Fig.8.4) shows the speed tracking response in the translational motion as well as the tracking error.

The plot at the left of (Fig.8.4) shows actual speed and reference speed versus time. The noise is larger in this case compared to others. But the actual speed does keep on track to the reference speed trajectory without obvious oscillation. On the right side of (Fig.8.4) shows the speed tracking error along time. It can be observed that the error is uniformly distributed, and it is bounded within 0.4 degree/sec and it cannot be reduced further due to the manufacturing quality of the gear trains and the effect of quantization error, which is discussed in the previous chapter.

(Fig.8.5) shows the step increments and decrements of the translational and rotational position. It can be seen that the error in both case are larger compared to the results shown before. This is because the results in (Fig.8.5) is achieved using a

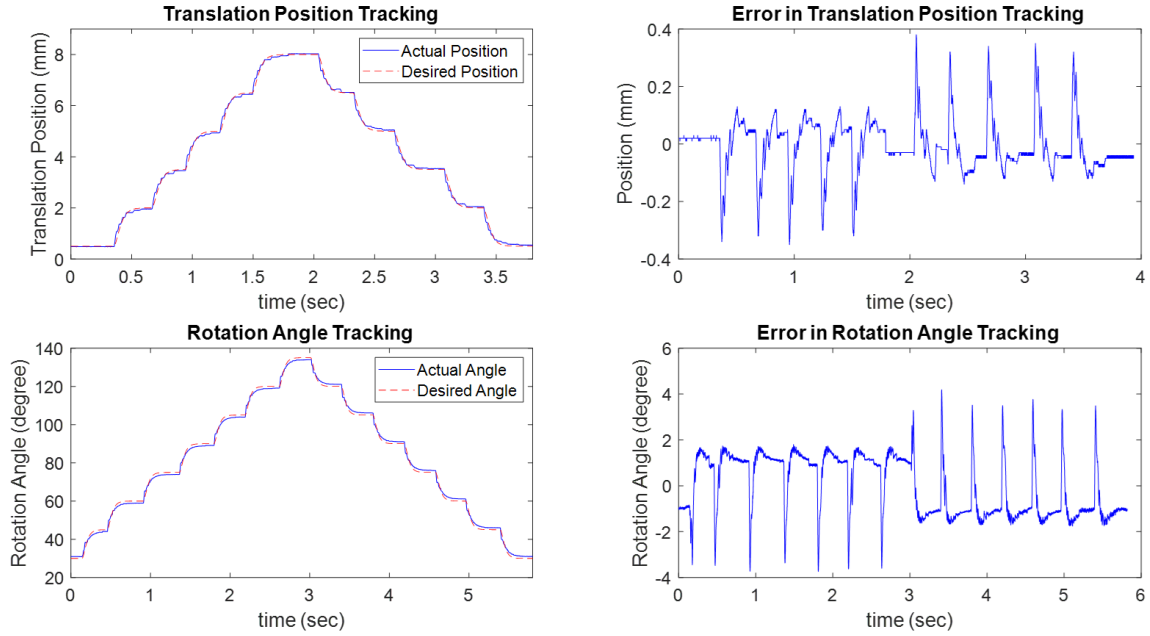


Figure 8.5. Stepping up and down in position tracking for the translational and rotational system when Kalman filter is not applied.

simple low pass filter rather than a model based Kalman filter. Thus reader should be able to see that the response without well-tuned Kalman filter tends to oscillate a lot due to the signal delay, and the steady state error is larger.

(Fig.8.5(a)) shows the position tracking of the translational motion for 7.5 mm of travel in step sizes of 1.5 mm. The solid line is the actual position of the instrument shaft and the dashed line is the desired position. In (Fig.8.5(b)) plots the errors for this test. The controlled rotation response is shown in (Fig.8.5(c)) for a rotation range of $\pm 115^\circ$ with incremental steps of 15° . The solid line is the actual angular position of the instrument shaft and the dashed line is the desired position. (Fig.8.5(d)) plots the errors over time.

A video of the system independently controlling the translation and rotation of two surgical instruments can be found here: https://youtu.be/47-AyobN0_U.

As a summary of this chapter, the error in the tracking is primarily due to the model structure/parameters uncertainty, the manufacturing quality and quantization

error. The parameter estimations in the system identification section is based on approximation and thus is not very accurate. The nonlinear frictions in both translation and rotation system are modeled to be the Coulomb friction. These mismatch in the model parameters and structure bring error into the system. Additionally, all the mechanical parts are manufactured using a 3D printer. Therefore, their mating surfaces are not smooth and the gear mating is also not good, which induces backlash problem. Moreover, the dimension error in the printed parts bring problems into the system, especially in the case of the 3D printed gears and rack systems. This also results in backlash that not only adds mechanical delay to the system but can also create large errors in both the transient and steady state. However, even with the errors that are present, the mechanical design of the system still functions as desired and is able to meet the specified design requirements.

9. FUTURE WORK

The performance of the device is as expected, but there are improvements can be made to have a more convenient, robust and accurate system.

In terms of overall design, another degree of freedom can be added to the system. Besides the independent rotation of the individual instrument shaft, the whole device could be potentially rotated by a specially design mechanism as shown in (Fig.9.1). The add-on system in grey color is a planetary gear train, in which the ring gear, or the outer shell, is fixed. One of the planet gears is driven by the motor fixed on the Robotic Cannula system, which is in yellow color; the other two planet gears are fixed on the shafts fixed on the Robotic Cannula system. The sun gear is concentric to the Robotic Cannula system as well as the ring gear, and it is free to rotate. When the motor is spinning, three planetary gears will spin around the sun gear, and thus the

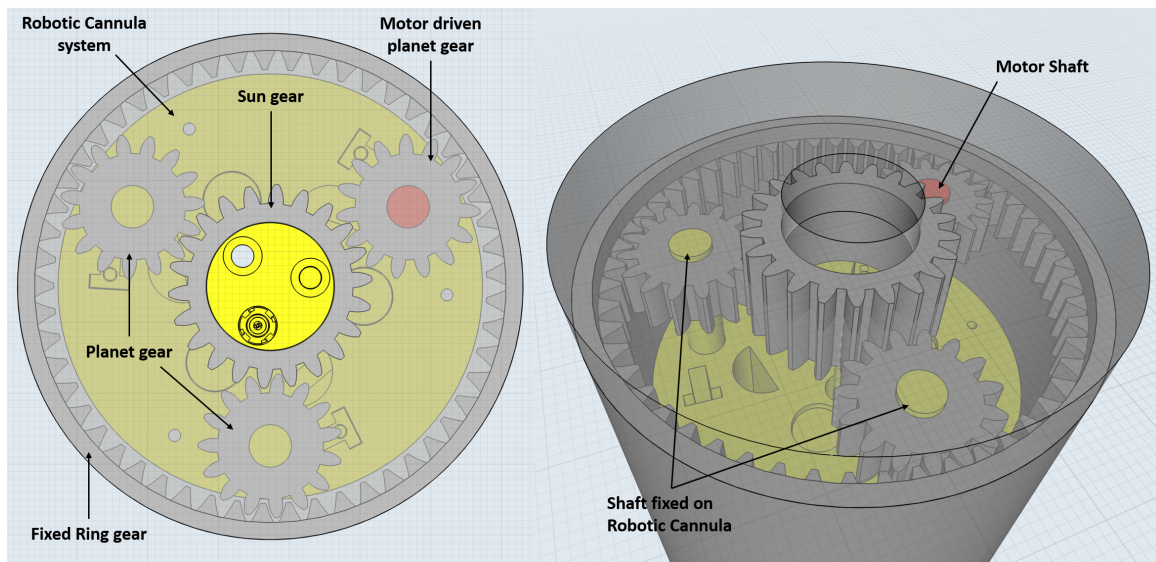


Figure 9.1. Future add-on design to enable the rotation of the Robotic Cannula system.

Robotic Cannula system is rotated. With this design, the surgeon will find it more easily to target a certain location in the work space. The giant planetary gear train can reduce the speed of the DC motor and increase the torque so that the rotation of the whole device can be done.

In terms of the manufacturing, rather than 3D printing the manufactured parts, they can be made with a CNC machine and out of metal to increase their dimensional accuracy, strength, and improve their surface finish. This will also make the system easier to model which will help with model-based control approaches.

In terms of the controller design, though sliding mode control guarantees a very small error, it can result in chattering of the mechanical system. Thus in the future, an adaptive robust controller could be designed to improve the system behavior. The sensors can also be upgraded to obtain more precise and less noisy measurements, and a current sensor could be potentially added to the system to make Kalman Filter state estimation more accurate. With these changes, the error in position and rotation tracking should be significantly reduced. Finally, the appropriate teleoperation controls for the surgeon to most effectively operate the system needs to be studied.

10. CONCLUSIONS

A robotic cannula system has been designed to independently control the axial position and rotation of up to three surgical instruments. It has been specifically designed for robotic lumbar discectomy procedures and the instruments developed in [20]. However, it is also designed to accommodate existing laparoscopic instruments.

The dexterity and precision of the developed robotic cannula system meets the requirements for performing robotic lumbar discectomy. It occupies a volume of approximately 123 cm^3 above the patient. During the surgery procedure, the robotic cannula will be rigidly mounted vertically above the patient, like a standard cannula in minimally invasive surgical procedures. The front cannula will be inserted into the patient body while the back cannula will reside outside the patient. The instruments will be inserted into the through the rear of the back cannula in order to reach the surgical workspace. The robotic cannula can then be teleoperatively controlled by the surgeon to independently position and rotate the instruments.

REFERENCES

REFERENCES

- [1] American Association of Neurological Surgeons. *Low Back Pain*, (accessed May 16, 2016). <https://www.aans.org/en/Patients/Neurosurgical-Conditions-and-Treatments/Low-Back-Pain>.
- [2] PhysioWorks. *Bulging Disc*, (accessed November 20, 2015). <http://physioworks.com.au/injuries-conditions-1/bulging-disc>.
- [3] A. J. Pugely, C. T. Martin, Y. Gao, and S. A. Mendoza-Lattes. Outpatient Surgery Reduces Short-Term Complications in Lumbar Discectomy. *Spine*, 38(3):264–271, February 2013.
- [4] M.D. William O. Reed, Jr. *Arthroscopic Microdiscectomy*, (accessed November 20, 2015). <http://www.handandspine.com/forms/AMDbrochure.pdf>.
- [5] P. L. Anderson, R. A. Lathrop, and R. J. Webster III. Robot-like dexterity without computers and motors: a review of hand-held laparoscopic instruments with wrist-like tip articulation. *Expert Review of Medical Devices*, 13(7):661–672, 2016. PMID: 26808896.
- [6] A. Adili. Robot-assisted orthopedic surgery. *Seminars in Laparoscopic Surgery*, 11(2):89–98, 2004.
- [7] R. H. Taylor and D. Stoianovici. Medical robotics in computer-integrated surgery. *IEEE Transactions on Robotics and Automation*, 19(5):765–781, 10 2003.
- [8] IntuitiveSurgical. *da Vinci Surgical System*, (accessed February 25, 2019). <https://www.intuitive.com/en/products-and-services/da-vinci>.
- [9] L. Ascari, C. Stefanini, U. Bertocchi, and P. Dario. Robot-assisted endoscopic exploration of the spinal cord. *Proceedings of the Institution of Mechanical Engineers, Part C: Journal of Mechanical Engineering Science*, 224(7):1515–1529, 2010.
- [10] MazorRobotics. *Renaissance Guidance System*, (accessed February 25, 2019). <https://mazorrobotics.com>.
- [11] GlobusMedical. *ExcelsiusGPS Robotic Navigation System*, (accessed February 25, 2019). <http://globusmedical.com/ExcelsiusGPS/>.
- [12] K. Ponnusamy, S. Chewning, and C. Moh. Robotic approaches to the posterior spine. *Spine*, 34(19):2104–2109, 2009.
- [13] S. Yang, H. J. Jin, M. K. Jae, C. Kim, S. Yi, Y. Ha, K. Nyun Kim, and D. Yoon. Current and future of spinal robot surgery. 7, 01 2010.

- [14] J. Y. K. Lee, B. W. O'Malley, J. G. Newman, G. S. Weinstein, B. Lega, J. Diaz, and M. S. Grady. Transoral robotic surgery of craniocervical junction and atlantoaxial spine: a cadaveric study. *Journal of Neurosurgery: Spine SPI*, 12(1):13–18, 2010.
- [15] M. Sool Yang, D. Yoon, K. Nyun Kim, H. Kim, J. Won Yang, S. Yi, J. Lee, W. Ju Jung, K. Rha, and Y. Ha. Robot-assisted anterior lumbar interbody fusion in a swine model in vivo test of the da vinci surgical-assisted spinal surgery system. *Spine*, 36:E139–43, 01 2011.
- [16] A. Menciassi, J. H. Park, S. Lee, S. Gorini, and P. Dario. Robotic solutions and mechanisms for a semi-autonomous endoscope. *IEEE/RSJ International Conference on Intelligent Robots and Systems*, 2(October):1379–1384, 2002.
- [17] N. Simaan, R. Taylor, and P. Flint. A dexterous system for laryngeal surgery. *IEEE International Conference on Robotics and Automation, 2004. Proceedings. ICRA '04. 2004*, 1:351–357, 2004.
- [18] M. Minor and R. Mukherjee. A Mechanism for Dexterous End-Effector Placement During Minimally Invasive Surgery, 1999.
- [19] DLR. *DLR MICA Surgical Instrument*, (accessed November 9, 2015). http://www.dlr.de/rmc/rm/en/desktopdefault.aspx/tabid-3829/6255_read-9015/.
- [20] B. Johnson, Z. Gong, B. Cole, and D.J. Cappelleri. Design of compliant 3d printed surgical end-effectors for robotic lumbar discectomy procedures. *ASME Journal of Mechanisms and Robotics*, to appear 2019, doi:10.1115/1.4042543.
- [21] H. Yamashita, K. Matsumiya, K. Masamune, H. Liao, T. Chiba, and T. Dohi. Two-DOFs bending forceps manipulator of 3.5-mm diameter for intrauterine fetus surgery: Feasibility evaluation. *International Journal of Computer Assisted Radiology and Surgery*, 1(SUPPL. 1):218–220, 2006.
- [22] S. N. Shaikh. Natural orifice transluminal surgery: Flexible platform review. *World Journal of Gastrointestinal Surgery*, 2(6):210, 2010.
- [23] G. Girish. *Laminectomy*, (accessed November 20, 2015). <http://www.drgguptaortho.com/spine-laminectomy.php>.
- [24] M. J. Perez-Cruet, K. T. Foley, R. E. Isaacs, L. Rice-Wyllie, R. Wellington, M. M. Smith, and R. G. Fessler. Microendoscopic lumbar discectomy: Technical note. *Neurosurgery*, 51(November):129–136, 2002.
- [25] R. William. *Arthroscopic microdiscectomy*, (accessed November 9, 2015). <http://www.spinedr.com>.
- [26] J. Sheng, X. Wang, T. L. Dickfeld, and J. P. Desai. Towards the development of a steerable and mri-compatible cardiac catheter for atrial fibrillation treatment. *IEEE Robotics and Automation Letters*, 3(4):4038–4045, Oct 2018.
- [27] M. Ruderman, J. Krettek, F. Hoffmann, and T. Bertram. Optimal state space control of dc motor. *IFAC Proceedings Volumes*, 41(2):57965801, 2008.

- [28] L. Kuentz, A. Salem, M. Singh, M. C. Halbig, and J. A. Salem. Additive manufacturing and characterization of polylactic acid (pla) composites containing metal reinforcements. 04 2017.
- [29] S. Gutman. Uncertain dynamical systems—a lyapunov min-max approach. *IEEE Transactions on Automatic Control*, 24(3):437–443, June 1979.
- [30] A. S. I. Zinober. Deterministic control of uncertain systems. In *Proceedings. ICCON IEEE International Conference on Control and Applications*, pages 645–650, April 1989.